ELSEVIER

Tectonophysics 331 (2001) 197–227

TECTONOPHYSICS

www.elsevier.com/locate/tecto

Lithologic tomography: an application to geophysical data from the Cadomian belt of northern Brittany, France

Miguel Bosch[a,1,*], Antonio Guillen[b,2], Patrick Ledru[b,3]

[a]*Laboratoire de Tomographie Géophysique, Institut de Physique du Globe de Paris, 4 place Jussieu, F75252, Paris Cedex 05, France*
[b]*BRGM, BP 6009, 45060 Orléans Cedex 02, France*

Received 15 April 1998; accepted 1 March 2000

Abstract

A probabilistic description of subsurface lithologic structures can be established by inverting multidisciplinary geophysical data constrained by geological and geostatistical priors. The methodology is based on the joint modelling of several media properties and on a statistical description of the relationships between them. The information provided by the geophysical data and the geological and geostatistical priors is represented by probability density functions (*pdf*) that are combined into a posterior *pdf* composed by: (1) a prior *pdf* in the space of the primary (lithologic) model parameters, (2) a *pdf* of the secondary (physical) model parameters conditional to the primary model parameters and (3) a joint likelihood function that is the product of the independent likelihood functions for each observed geophysical field. Applying a Markov chain sampling method enables a large sample of joint models to be generated from the posterior *pdf*. The true configuration of the media is then determined from the representation of models pulled from the chain and the elaboration of statistics from the large sample of posterior joint models. The method was used to invert gravity and magnetic data jointly characterising the mass density field, the magnetic susceptibility field and the lithotype field along two 2-D sections of the geological units in the Cadomian belt of northern Brittany. Besides generating 10^6 joint models consistent with the observations and priors, some features of the joint models and the statistical tomographic images provided additional insights to the geologic configuration of the area. For example, the Main Cadomian Thrust shows an irregular geometry that could have resulted from the belt emplacement and/or from Variscan tectonism, and the Hercynian granitic intrusion shows a deep subsurface continuation. The cosimulation of magnetic susceptibility and mass density inside each lithologic region was performed according to a multivariate Gaussian model or a mixed multivariate Gaussian functions model that was developed specially to describe multimodal distributed properties.

Keywords: lithologic tomography; joint inversion; multidisciplinary surveys; upper crust; geophysical methods; stratigraphic inversion

* Corresponding author. Address: Earth Sciences Department, Bullard Laboratories, University of Cambridge, Madingley Road, Cambridge, CB3 0EZ, UK. Tel.: +44-1223-337-102; fax: +44-1223-360779.

E-mail addresses: bosch@esc.cam.ac.uk (M. Bosch), mbosch@reacciun.ve (M. Bosch), a.guillen@brgm.fr (A. Guillen), p.ledru@brgm.fr (P. Ledru).

[1] Present address: Departamento de Fisica Aplicada, Facultad de Ingeniería, Universidad Central de Venezuela, Venezuela. Fax: +58-2-286-66-36.

[2] Fax: +33-2-38-64-33-34.

[3] Fax: +33-2-38-64-47-02.

0040-1951/01/$ - see front matter
PII: S0040-1951(00)00243-2

1. Introduction

Ambitious programs have recently been developed to image structures of the upper-crust in three dimensions (3-D); examples are the GeoFrance-3D program (Ledru, 1997), the German KTB program (Emmermann and Lauterjung, 1997), and the Canadian Lithoprobe program (Clowes et al., 1992). A common aspect of all these programs is the multidisciplinary effort to provide information enabling the interpretation and imaging of the structures in the region studied. The different kinds of data that are collected and processed include, among others, geological field data, borehole samples, petrophysical and petrochemical studies on samples, and seismic, gravity, magnetic and electromagnetic surveys. One idea behind this effort is that a large amount of high-quality and diverse information, together with more advanced interpretation methods, can lead to a reliable 3-D imaging of the complex upper-crust structures.

In this article, we describe a new method of inferring the major lithologic structure of an area through integrating the large amount of diverse data generated by multidisciplinary surveys and exploration programmes. The method, based on a probabilistic formulation of the inference of lithologic media characteristics from: (1) geological prior information; (2) petrophysical and geostatistical prior information; and (3) geophysical observations, involves the joint representation and parameterization of the different media properties.

The mathematical framework needed to formalize the inverse problem requires the representation of the information as probability density functions (*pdf*) defined over the model parameter space; the posterior *pdf* represents the combination of the available information. The inference is performed by: (1) generating joint model outcomes from the posterior *pdf*; (2) observing these models; and (3) calculating statistics from a large number of them. The samples from the posterior *pdf* are obtained by a Markov chain-sampling algorithm adapted to the structure of the posterior *pdf* (see detailed discussion on the methodology and its theoretical foundations in Bosch, 1999).

The method has been applied to data from the Cadomian belt of northern Brittany (France) to infer the two-dimensional (2-D) organization of several major lithotypes. This region represents an eroded mountain chain that formed from the Cadomian collision between a volcanic arc system and the continental crust (Brun and Balé, 1990; D'Lemos, 1990), and was later submitted to significant shear faulting and intrusions during the Variscan orogeny. The geophysical data to be inverted were gravity and magnetic profiles.

2. General description of the method

A primary difference between lithologic tomography and conventional tomography resides in the media description. For lithologic tomography one introduces an explicit description of the media lithology into the model, along with the description of several physical properties related to the geophysical data. The physical media properties are used to explain specific physical phenomena; for example, magnetic susceptibility is relevant for magnetic observations but not for seismic wave propagation. Hence, physical properties provide only a partial description of the medium and its geophysical response. By characterizing the lithology in the models, in addition to the representation of physical properties, we obtain a media description that is closer to its actual structure and common to all the observations. Another difference between this strategy and conventional tomography is that it allows the joint inversion of different types of geophysical observation.

A hierarchy is established among the properties in terms of primary properties (lithology) and secondary properties (media physics); the secondary properties are determined from the available geophysical data. Physical properties explicitly involved in the forward calculation of the geophysical data obviously need to be included in the joint model; for instance, if gravity data are included, the mass density should be among the secondary properties.

The choice of primary properties is determined by two criteria: (1) they should be useful for discriminating and characterizing the lithology or the media conditions; and (2) the secondary properties should be statistically dependent on them. These two criteria are commonly met because physical rock properties are dependent on lithology and, in most cases, this dependence can be statistically described by analysis

of the rock sample data. Suitable selection of the primary properties also depends on the exploration context; for example, in some cases the definition of lithotypes may be the best way to characterize the lithology, whereas in other cases it may be more appropriate to use iron content and temperature to characterize the Earth's mantle media. Then again, when dealing with sedimentary environments, the physical rock properties are highly dependent on porosity and fluids, and so these parameters should possibly be considered in addition to the lithotype for the primary media description.

The objective of our method is to infer several media properties within the Earth volume Ω under study. The properties can be categorical (such as lithotype) or continuous (such as mass density, magnetic susceptibility and temperature) — in our application of the method to the Cadomian belt, the properties considered were lithotype, mass density and magnetic susceptibility.

The spatial distribution of a media property within Ω is described by a property field $z_1(\mathbf{x})$ with $\boldsymbol{x} \in \Omega$ being the continuous coordinate position. The field $z_1(\mathbf{x})$ is currently represented by a model in terms of a finite number of model parameters $\mathbf{m}_1$. Field models are often based on partitioning the space into piecewise homogeneous elements — in the Cadomian belt application we used homogeneous prisms of triangular section. Other common field models consist in defining an interpolation rule and the properties over a grid of points, or in defining the field in terms of a base of functions. The joint description of several media properties, say N, is given by the joint property field $z(x) = \{z_1(x), z_2(x), \ldots, z_N(x)\}$, or equivalently by the corresponding joint array of model parameters $m = \{m_1, m_2, \ldots, m_N\}$. The joint model parameter space (i.e. the space containing $\mathbf{m}$) is denoted by M.

In distinguishing between primary and secondary media properties, we induce a partition of the joint model parameter space M that can be represented as the product space of a primary model parameter space and a secondary model parameter space, i.e. $M = M_{\text{pri}} \times M_{\text{sec}}$. Considering primary media properties, K, the primary array of model parameters is denoted $m_{\text{pri}} = \{m_1, m_2, \ldots, m_k\}$, and the secondary array of model parameters is denoted $m_{\text{sec}} = \{m_{k+1}, \ldots, m_N\}$. By specifying the values of m_{pri} and m_{sec}, one describes the primary property fields (lithology) and the secondary property fields (physical properties), respectively.

The different types of information concerning the media properties and their spatial organization can be represented by *pdf* defined over the model parameter spaces. The types of information entering the inverse problem considered here are geological prior information concerning the media lithology, petrophysical and geostatistical prior information concerning the physical media properties, and the likelihood concerning the geophysical observations. The inference consists in combining these information components; the combined information is represented by the posterior probability density $\sigma(\mathbf{m})$. For the lithologic tomography problem, the structure of the posterior probability density is given by (Bosch, 1999) as:

$$\sigma(\mathbf{m}_{\text{sec}}, \mathbf{m}_{\text{pri}}) = c\ \theta_{\text{s|p}}(\mathbf{m}_{\text{sec}}|\mathbf{m}_{\text{pri}})\ \rho_{\text{p}}(\mathbf{m}_{\text{pri}})\ L(\mathbf{m}_{\text{sec}}) \quad (1)$$

Each term of the above expression represents a different component of the information:

(1) The prior information about the lithologic media structure is described by the probability density $\rho_{\text{p}}(\mathbf{m}_{\text{pri}})$, defined over the primary model parameter space. It represents geological prior knowledge of the area, constraining, for instance, the lithotypes present, their position at the surface ($z = 0$) and their geometric relationships.

(2) The term $\theta_{\text{s|p}}(\mathbf{m}_{\text{sec}}|\mathbf{m}_{\text{pri}})$ is a conditional probability describing the information on the secondary media properties, their spatial relationships, their cross-relationships and their dependence on the primary properties. This density summarizes information from the petrophysical and geostatistical prior data.

(3) The term $L(\mathbf{m}_{\text{sec}})$ is the joint likelihood function that measures the probability misfit between the data calculated from the joint model and the geophysical observations.

(4) The factor c is a normalization constant.

The form of $L(\mathbf{m}_{\text{sec}})$ in Eq. (1) depends on the observations and the type of uncertainties concerning the observed data, as well as on the errors in the calculation of the geophysical fields. For the inference problem based on multiple geophysical information, the likelihood function can be factored by assuming that the observational uncertainties and calculation errors are independent across the geophysical

methods (Bosch, 1999), i.e.:

$$L(\mathbf{m}_{\text{sec}}) = \prod_{m=1,M} L_m(\mathbf{m}_{\text{sec}}), \quad (2)$$

where the independent terms $L_m(\mathbf{m}_{\text{sec}})$ are the likelihood function for each geophysical method.

The assumption of the independence of observational uncertainties and calculation errors across geophysical methods is realistic in most situations. The sources of observational error (instrumental, human, corrections, positioning) are commonly different for different geophysical techniques and surveys, and the forward data calculations are commonly performed following different equations, algorithms and methods.

When dealing with geophysical inverse problems, the terms in Eqs. (1) and (2) are generally complicated functions. For example, the likelihood functions $L_m(\mathbf{m}_{\text{sec}})$ involve the solution of non-linear forward problems, the prior density $\rho_{\text{p}}\mathbf{m}_{\text{pri}})$ follows a statistically inhomogeneous model (prior statistics being dependent on coordinate position $x \in \Omega$), and the conditional *pdf* $\theta_{\text{s}|\text{p}}(\mathbf{m}_{\text{sec}}|\mathbf{m}_{\text{pri}})$ involves: (a) the relationship between the primary and secondary property fields, (b) the spatial relationships of the secondary properties at different positions and (c) the cross-relationships between the secondary properties. In addition to these complexities, the model parameter space has a large number of dimensions — in the Cadomian belt application, the number of model parameters was around 2000.

Because of these complexities, the posterior density $\sigma(\mathbf{m})$ does not have a closed form expression and its integration, to obtain probabilities, has to be performed according to well-established statistical techniques. Such techniques consist in generating joint model outcomes from $\sigma(\mathbf{m})$ in order to estimate, from a large sample collection of these outcomes, the desired posterior information statistics (probabilities, expected values, marginal or conditional histograms, identification of clusters, etc.). For this we use a Markov chain sampling method; a Markov chain over the space M can be regarded as the record of a pseudo-random walk in M, producing a model outcome at each step t of the walk, until a final step T. The Markov chain is said to be *ergodic* to a *pdf* $\pi(\mathbf{m})$ if any set of model outcomes from the chain $S^T = \{\mathbf{m}^1, \mathbf{m}^2, \ldots, \mathbf{m}^T\}$ converge to a sample from $\pi(m)$ as the number of steps increases. Different methods are available to construct Markov chains ergodic to an arbitrary *pdf* $\pi(\mathbf{m})$; the two best-studied ones being the Metropolis sampler and the Gibbs sampler (see reviews on Markov chain samplers in Tierney, 1994; Besag et al., 1995). The sampling method is here specially adapted to the structure of the posterior density to follow three stages corresponding with the three terms in Eq. (1);

- *Primary chain*. The first stage consists in generating a primary chain of lithologic models representative of the geological prior information (i.e. a Markov chain ergodic to the prior density $\rho_{\text{p}}(\mathbf{m}_{\text{pri}})$). Such an algorithm can be implemented by applying perturbation rules to the primary model parameters or using algorithms such as the Metropolis or Gibbs samplers.
- *Prior chain*. The second stage consists in generalizing the primary chain to a chain in the joint model parameter space by generating secondary model parameters from the conditional *pdf* $\theta_{\text{s}|\text{p}}(\mathbf{m}_{\text{sec}}|\mathbf{m}_{\text{pri}})$ Given the outcome $\mathbf{m}^t_{\text{pri}}$ for an arbitrary step t of the primary chain, the outcome $\mathbf{m}^t = \{\mathbf{m}^t_{\text{sec}}, \mathbf{m}^t_{\text{pri}}\}$ is defined by sampling $\mathbf{m}^t_{\text{sec}}$ from $\theta(\mathbf{m}_{\text{sec}}|\mathbf{m}_{\text{pri}})$. The Markov chain constructed in this way is *ergodic* to the joint prior probability density $\theta_{\text{s}|\text{p}}(\mathbf{m}_{\text{sec}}|\mathbf{m}_{\text{pri}})\rho_{\text{p}}(\mathbf{m}_{\text{pri}})$. The joint models generated by this chain are representative of all the prior information introduced to the problem (geological, petrophysical and geostatistical).
- *Posterior chain*. The final stage consists in modifying the prior chain to generate a Markov chain ergodic to the posterior density $\sigma(\mathbf{m})$. The joint models generated by this chain are representative of the prior information constrained by the likelihood with the geophysical observations. This stage is constructed following the method described in the work of Mosegaard and Tarantola (1995) based on the Metropolis algorithm (Metropolis et al., 1953). A brief description of the Metropolis algorithm is given in Appendix A.

3. Implementation of the method to the Cadomian belt

The area under study and eight major lithotype regions represented in a preliminary 3-D model are shown in Fig. 1. The inversion method was

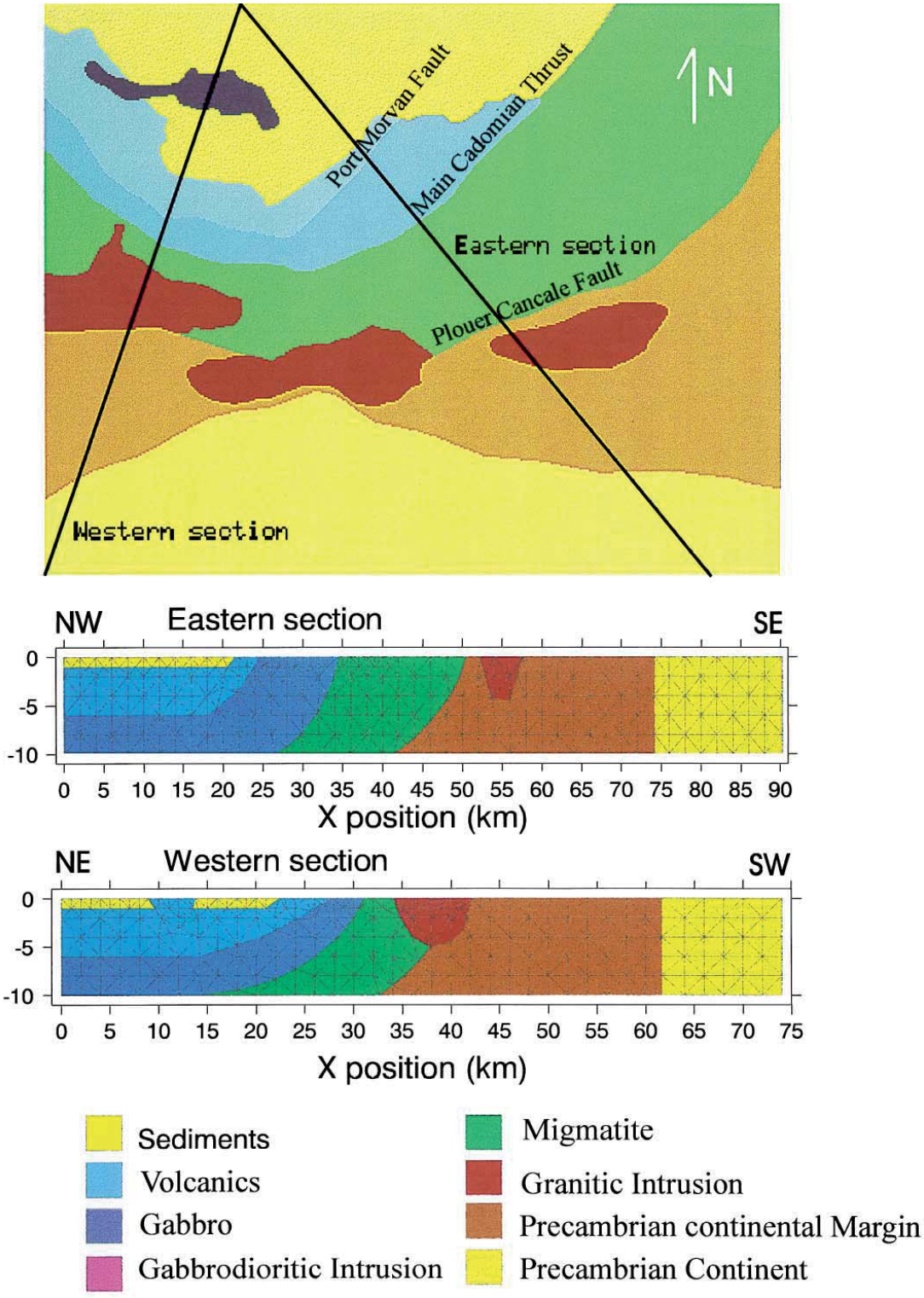

Fig. 1. Plan view and two cross-sections of a preliminary 3-D model of the studied area. The lines in the sections show the triangular network used to model the media property fields.

implemented for two vertical 2-D sections, designated as *Eastern section* and the *Western section*, intersecting this model. The region is covered by gravity and magnetic data, which were interpolated to provide data along the two section profiles and used to define the likelihood function.

The realistic description of joint models in 3-D requires a larger number of model parameters than for joint models in 2-D. Although the ultimate goal is to apply the method in 3-D, the implementation in 2-D was chosen here to test both the methodology and different algorithmic approaches in a favourable computing situation.

The secondary properties selected to be represented in the joint model were mass density (related to the gravity data) and magnetic susceptibility (related to the magnetic data). As these properties have a log–normal distribution, logarithmic transformation of the property was used systematically in the simulations to give a better representation of the property variability. The logarithm of the mass density is denoted ρ^* and that of the magnetic susceptibility is denoted k^*; the base 10 logarithm has been used for the illustrations to make it easier to relate the transformed and non-transformed property values.

The primary property represented in the joint model was the lithotype. Classification of the rocks into lithotypes was based on conventional geological classification and also on the statistical characterization of the secondary properties for each geological entity. In this way, several neighbouring geological entities could be integrated into the same lithotype as long as the statistical characteristics of their secondary properties were similar. Neighbouring lithotypes, however, should exhibit differences in the behaviour of the secondary properties in order to be discriminated by the geophysical data.

The study area represents a complete section through the Cadomian belt that resulted from collision between the volcanic arc system of the Domnonean domain to the north and the continental basement of the Mancellian domain to the south (Chantraine et al., 2001). The overall geological infrastructure of the eroded belt is represented by the following lithologic types within the main tectonic units:

- The Saint-Brieuc Unit, made up essentially of magmatic and volcanic rocks of juvenile affinity, including ultrabasic, basic and acid rocks. It is schematized in Fig. 1 by a column composed of 'gabbro' and 'volcanics' overlain by 'sediments'. A 'gabbrodiorite intrusion' is found in the northeastern part of the area.
- The Guimgamp and Saint-Malo units, composed predominantly of migmatite and highly tectonized rocks marking the involvement of the continental margin in the collision belt. They are considered as a continental derived 'migmatite' lithotype.
- The Fougères Unit, corresponding to the outer domain of the Cadomian orogeny, weakly deformed by Cadomian tectonism. It is presented as the 'Precambrian continental margin'.
- The Central Armorican Domain, presenting a predominantly NeoProterozoic and Palaeozoic cover sequence resting over a basement corresponding to a 'Precambrian continent'.
- 'Granite intrusion', which occurred during the Variscan orogeny, mainly located along the North Armorican Shear Zone lineament.

The boundaries of these lithotypes, as shown in Fig. 1, were taken from the geologic map of the area (Chantraine et al., 2001) and were maintained fixed during the inversion.

Analysis of the available petrophysical data showed that the secondary properties of the rocks from the gabbrodiorite intrusion in the northeastern part of the area were similar to the secondary properties of other samples from the neighbouring volcanics, and these were therefore modelled as a single region (see the Western section in Fig. 1). Although the Precambrian continental margin of the Fougères Unit and the Precambrian continent of the Central Armorican Domain do not show marked differences in either the secondary properties or the observed gravity and magnetic data, they were modelled separately in view of the significance of the geological boundary.

The description of the property fields was based on a triangulation of the 2-D surface of the sections; the media were considered to be integrated by homogeneous, laterally infinite, prisms of triangular section. The number of vertexes and prisms (triangles) for each section do not change during the inversion. The model parameters were thus:

(1) the position of the triangle vertexes;
(2) the lithotype of each triangle;
(3) the mass density ρ^* of each triangle;
(4) the magnetic susceptibility k^* of each triangle.

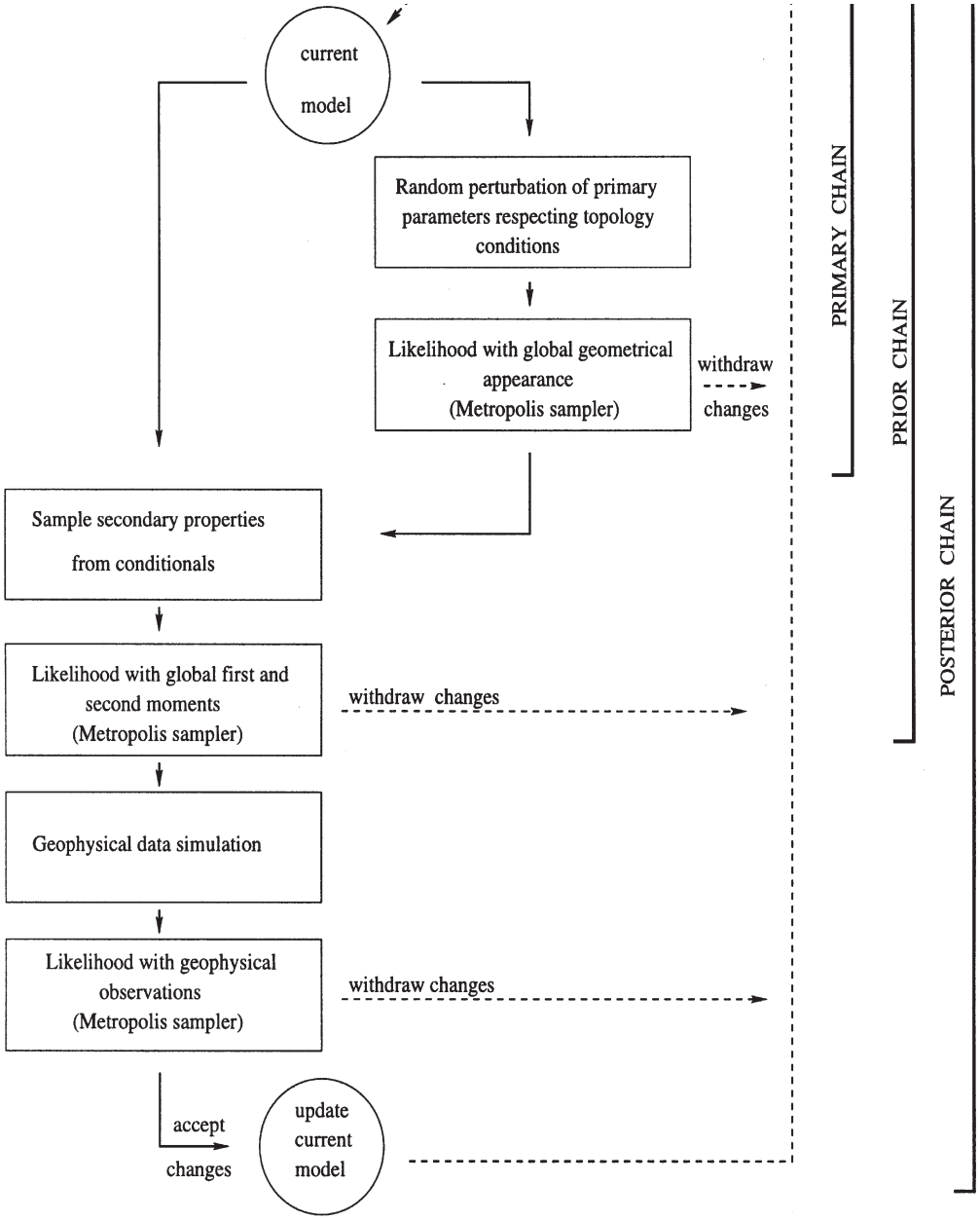

Fig. 2. Diagram of the major functions of the algorithm for one step of the posterior chain. The posterior chain includes the prior chain functions that in turn include the primary chain functions. Solid arrows indicate the forward flow direction of the algorithm; dashed arrows indicate returns to initiate a new iteration.

3.1. Prior sampling of the lithologic models

The prior information about the lithologic regions filling the 2-D section provided an important constraint in the freedom of the lithologic model. The lithologic regions established in the initial models, shown in Fig. 1, were maintained connected to avoid their separation into multiple parts, and were kept constant at the surface ($z = 0$). Two parameters were used to control the relative size and shape of the regions: (1) the logarithm of the volume (logarithm of the area in 2-D) occupied by each lithotype, which

was used to control the expected relative representation and its dispersion; and (2) an aspect ratio of each lithologic region (perimeter divided by the square root of the area), which was used to control the appearance of the region's frontiers (**s**mooth or dendritic). To summarize, the prior information used in the simulation of the lithologies was:

(1) the lithotype: this was considered to be known at the surface and so the lithotype for triangles bounding the surface ($z = 0$) was fixed;

(2) the initial topology of the lithologic regions: this was maintained constant so that lithologic regions could not be eliminated, disconnected in two or more parts, or created;

(3) the volume and aspect ratio as well as their dispersion: these were provided in order to guarantee the same prior information on these parameters across lithotypes; for the Cadomian belt these parameters were identical for all the lithotypes, providing a priori the same expected volume fraction (1/7) and the same expected boundary smoothness (aspect ratio of $6/\sqrt{2}$) for the seven lithotypes considered in the lithologic model.

The models used to initiate the sampling chains were those shown for the Eastern and Western sections in Fig. 1, where the lithologic regions were obtained by intersecting the previously triangulated vertical plane with the preliminary 3-D model. These initial models defined the geometrical network of the model (vertexes, triangles and external boundaries) and provided the prior information about the regional topology and surface lithology to be preserved all along the inversion. No other information from the initial models was introduced in the prior information for this application.

The first stage, through sampling joint models from the posterior *pdf*, was to construct a chain generating primary (lithotype) models according to the geological priors of the area. This was done in two steps (Fig. 2): a first step of setting-up a Markov chain consistent with items 1 and 2 of the prior information enumerated above, and a second step incorporating item 3 using a Metropolis sampler. Starting with the initial model, the first step consisted in applying random perturbations to the primary model parameters, respecting certain conditions to guarantee that the surface lithology was not changed in the model and that the initial regional topology was not violated. To illustrate the procedure, consider that the chain is at step t with the primary model $\mathbf{m}_{\mathrm{pri}}^{t}$; then the next model outcome ($\mathbf{m}_{\mathrm{pri}}^{t+1}$) from the chain was obtained by alternatively applying one of the following perturbation rules over $\mathbf{m}_{\mathrm{pri}}^{t}$:

- *Vertex move.* Randomly select a vertex in the model and randomly move its position. In this operation, conditions were verified to avoid triangle overlapping.
- *Lithologic invasion.* Randomly select a triangle in the frontier between two lithologic regions and assign to this triangle the lithotype of the neighbour region. In this operation, conditions were verified to avoid any disconnection of regions or change of lithotype in a triangle bounding the surface ($z = 0$).

To maintain the correct position of the section's external boundaries, the vertexes in these external boundaries were not allowed to move. This did not apply to the vertexes at the surface ($z = 0$) that did not represent boundaries between lithotype regions; these could move horizontally to provide better model spatial resolution near the surface.

The second step consisted in incorporating the prior information about the global appearance of the region (described in item 3 above). This step was needed in order to simulate the desired smoothness of the frontiers between lithotypes and the desired volume fractions. For this purpose the perturbed model was subjected to a Metropolis sampling rule using a Gaussian function as likelihood function. The function was centred in the expected logarithm values of the volume and aspect ratio; the dispersion of the likelihood used in the Gaussian model made it possible to graduate (as desired) the weight of this component of the prior information in the simulated lithologic models.

3.2. Prior sampling of the joint models

The algorithm used for the prior sampling of the lithologic models concerns the generation of primary property fields. Secondary property fields were then generated from the conditional probability density $\theta_{\mathrm{s|p}}(\boldsymbol{m}_{\mathrm{sec}}|\boldsymbol{m}_{\mathrm{pri}})$ and the primary model parameters $\boldsymbol{m}_{\mathrm{pri}}$ to generalize the primary chain to a prior chain in the joint model space.

The secondary model parameters consisted of the mass density Ω_{gab}, and the magnetic susceptibility

k^* for each triangle. To describe the spatial relationships between these parameters, the values of ρ^* and k^* were assigned to a point located at the centre of the triangle; each time the vertexes of the triangle were moved, the position of the centre was updated.

Secondary properties within each lithotype region were considered to be statistically homogeneous and two different models were used for the conditional *pdf* $\theta_{s|p}(\mathbf{m}_{sec}|\mathbf{m}_{pri})$. To illustrate this, we can consider the case of a simulation inside the gabbro lithotype region Ω_{gab}, with secondary model parameters $\mathbf{s}_{gab}$ defined on the centres $\mathbf{x}_n$ of triangles inside Ω_{gab} :

$$s_{gab} = \{\rho^*(\mathbf{x}_1), \ldots, \rho^*(\mathbf{x}_N), k^*(\mathbf{x}_1), \ldots, k^*(\mathbf{x}_N)\} \quad (3)$$

with $x_n \in \Omega_{gab}$.

A first model for the conditional *pdf* was the multivariate Gaussian model, widely used in geostatistical work:

$$\theta_{s|p}(\mathbf{m}_{sec}|\mathbf{m}_{pri}) \propto \exp[-\tfrac{1}{2}(\mathbf{s}_{gab} - \bar{\mathbf{s}}_{gab})^t \mathbf{C}_{gab}^{-1}(\mathbf{s}_{gab} - \bar{\mathbf{s}}_{gab})], \quad (4)$$

with $\mathbf{C}_{gab}$ being the covariance matrix and $\bar{\mathbf{s}}_{gab}$ the mean values of the secondary parameters. The model used for the covariance function was Gaussian with a range of 3 km for all the lithotypes with the exception of the volcanics (0.5 km) and gabbro (2 km).

The sampling process of the secondary model parameters was performed by perturbing the mass density ρ^* and the magnetic susceptibility k^* in a single triangle at each step following a method of simulation by the conditionals of Eq. (4). The conditionals for the secondary properties of the triangle centred in the coordinate position $\mathbf{x}_N$ are given as:

$$\begin{cases} \theta_1(\rho^*(\mathbf{x}_N)\Big|\rho^*(\mathbf{x}_1), \ldots, \rho^*(\mathbf{x}_{N-1}), k^*(\mathbf{x}_1), \\ \times \ldots, k^*(\mathbf{x}_{N-1})) \propto \exp\left[\dfrac{-(\rho^*(\mathbf{x}_N) - \rho_c^*)^2}{2\sigma_{c\rho}^2}\right], \\ \theta_2(k^*(\mathbf{x}_N)\Big|\rho^*(\mathbf{x}_1), \ldots, \rho^*(\mathbf{x}_{N-1}), k^*(\mathbf{x}_1), \\ \times \ldots, k^*(\mathbf{x}_{N-1})) \propto \exp\left[\dfrac{-(k^*(\mathbf{x}_N) - k_c^*)^2}{2\sigma_{ck}^2}\right] \end{cases} \quad (5)$$

with $\rho_c^*, \sigma_{\rho c}^2, k_c^*$ and σ_{ck}^2 being the simple cokriging estimates of $\rho^*(\mathbf{x}_N)$, $k^*(\mathbf{x}_N)$ and their corresponding variances (Deutsch and Journel, 1992); these parameters can be found solving a linear system of equations.

A second model, specially derived in this work to simulate multimodal distributed secondary properties within a lithotype region, consisted in a mixture of multivariate Gaussians:

$$\theta_{s|p}(\mathbf{m}_{sec}|\mathbf{m}_{pri}) \propto \sum_i a^i \exp[-\tfrac{1}{2}(\mathbf{s}_{gab} - \bar{\mathbf{s}}_{gab}^i)^t (\mathbf{C}_{gab}^i)^{-1} \times (\mathbf{s}_{gab} - \bar{\mathbf{s}}_{gab}^i)], \quad (6)$$

with $\mathbf{C}_{gab}^i$ and $\bar{\mathbf{s}}_{gab}^i$ being the covariance matrix and the centroid of each mode i and a^i being Real positive coefficients. The conditionals for this mixed Gaussian function are also mixed Gaussian and are given by

$$\begin{cases} \theta_1(\rho^*(\mathbf{x}_N)\Big|\rho^*(\mathbf{x}_1), \ldots, \rho^*(\mathbf{x}_{N-1}), k^*(\mathbf{x}_1), \\ \times \ldots, k^*(\mathbf{x}_{N-1})) \propto \sum_i b^i \exp\left[\dfrac{-(\rho^*(\mathbf{x}_N) - \rho_c^{*i})^2}{2(\sigma_{c\rho}^i)^2}\right], \\ \theta_2(k^*(\mathbf{x}_N)\Big|\rho^*(\mathbf{x}_1), \ldots, \rho^*(\mathbf{x}_N), k^*(\mathbf{x}_1), \\ \times \ldots, k^*(\mathbf{x}_{N-1})) \propto \sum_i c^i \exp\left[\dfrac{-(k^*(\mathbf{x}_N) - k_c^{*i})^2}{2(\sigma_{ck}^i)^2}\right] \end{cases} \quad (7)$$

with ρ_c^{*i}, $(\sigma_{c\rho}^i)^2$, k_c^{*i} and $(\sigma_{ck}^i)^2$ being the simple cokriging estimates of $\rho^*(\mathbf{x}_N)$ and $k^*(\mathbf{x}_N)$ for each mode i and its corresponding variances. Coefficients b^i and c^i can be obtained through evaluating Eqs. (6) and (7) in the cokriging estimates for each mode and solving two $I \times I$ systems of equations with I being the number of modes.

The sampling of secondary properties for a triangle from the conditionals (5) or (7), were performed in the prior chain:

- whenever the lithotype of a triangle was changed in the primary chain, and
- by randomly selecting any triangle in the model.

Before renewing the secondary properties in the triangle, the candidate modifications were passed

through a Metropolis step (see Fig. 2) to control a likelihood with the global first and second moments of the secondary properties (including the correlation between mass density and magnetic susceptibility) for each lithotype. A dispersion of one standard deviation of 10% of the first and second moments of the standardized secondary properties was used in all the results. In the case of multimodal simulation, the fraction of triangles in each mode was also controlled. The likelihood function of the Metropolis step was a Gaussian function centred in the expected standardized values of the controlled global parameters.

The control of the first and secondary moments by a Metropolis step helps centre the conditional simulation in the global priors. In particular, the secondary properties in the posterior chain may be deviated from its priors in order to explain the geophysical data. This deviation is constrained by the likelihood function under consideration and can be graduated as desired with the dispersion used in the Gaussian model of the likelihood.

The available petrophysical data for the area were collected for conventional interpretation purposes, which is why some lithotypes in the south of the model were not represented. In addition, the available data were not sufficient to characterize the spatial variability of the properties inside a lithological region. Nevertheless, a significant number of samples was collected for the volcanics and gabbro lithotypes that are the major sources of geophysical anomalies in the region. Examination of these data showed the presence of multimodality in the distributions of the secondary properties and provided the base for a realistic characterization of the media. Petrophysical data for the granite intrusions were taken from data on Canadian granites.

3.3. Posterior sampling of the joint models

The gravity profiles were interpolated at 1-km intervals from the residual Bouguer Anomaly map ($d = 2.7$ onshore, $d = 2.2$ offshore) data compiled by Truffert et al. (2001). These data already included a correction from a smooth regional component accounting for the gravity contribution of deep sources such as the Moho discontinuity. The magnetic data were obtained from two independent sets of data at elevations of 450 and 3000 m. The 450-m-altitude data was compiled by Galdeano et al. (2001) and were interpolated at regular intervals of 0.5 km along the section profile. The 3000-m-altitude data were sampled from a local, reduced to the pole, total field anomaly map (BRGM/CGG, France) obtained by reprocessing original data of the 'Levé Aéromagnétique Général de la France' (Le Mouël, 1969; Le Borgne and Le Mouël, 1969), where the lateral distance between the original profiles was 10 km.

The observation uncertainties used for the geophysical data along the profiles of the two sections were assumed to be Gaussian and spatially independent, with standard deviations of $\sigma_g = 0.5$ mgal for the gravity data, $\sigma_{450} = 10$ nT for the 450-m-altitude magnetic data and $\sigma_{3000} = 15$ nT for the 3000-m-altitude magnetic data. The expression of the likelihood function used was:

$$L(\mathbf{m}) = \exp\left[- \sum_{i=1,\dots,I} \frac{(d_i^{\mathrm{cal}} - d_i^{\mathrm{obs}})^2}{2\sigma_g^2} - \sum_{j=1,\dots,J} \frac{(d_j^{\mathrm{cal}} - d_j^{\mathrm{obs}})^2}{2\sigma_{450}^2} - \sum_{k=1,\dots,K} \frac{(d_k^{\mathrm{cal}} - d_k^{\mathrm{obs}})^2}{2\sigma_{3000}^2} - \right], \quad (8)$$

where $d_i^{\mathrm{obs}}, d_j^{\mathrm{obs}}$ and d_k^{obs} are, respectively, the gravity data, the 450-m-altitude magnetic data and the 3000-m-altitude magnetic data interpolated to the profile; the term within the brackets is called the joint data misfit.

The assumption of Gaussian spatially independent data errors was not supported by a specific study of the data. More complicated models for the likelihood function could be used if justified by an analysis of data uncertainties.

The data were calculated from the joint models by superposing the contributions of all the homogeneous prisms represented in the section; after a model perturbation, only the contribution of the changed prisms needed to be updated. The forward calculation of the gravitational field due to a prism was done by the method of Chapman (1979) and the forward calculation of the magnetic field by the method of Bott (1963). These methods provide the exact physical solution of the fields due to a polyhedron with

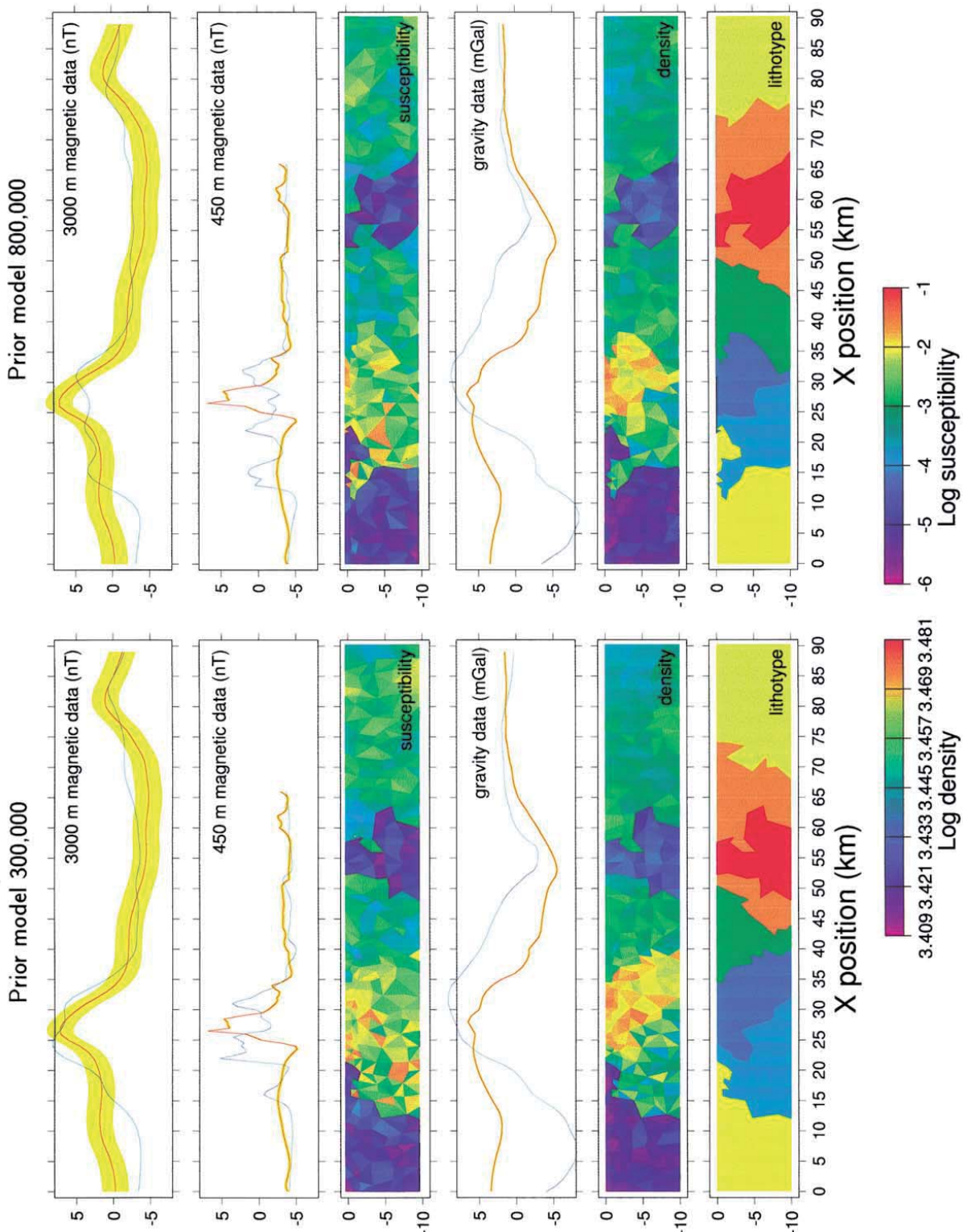

Fig. 3. Prior joint models 300 000 and 800 000 pulled from the 10^6 joint model chain sampling the prior *pdf* for the Eastern section. Lithotype colour codes are the same as in Fig. 1. The secondary properties are the base 10 logarithm of the mass density (kg/m^3) and the base 10 logarithm of the magnetic susceptibility (SI units). Calculated data are shown with a blue line and observed data with a red line; the yellow band indicates ±1 standard deviation uncertainty in the observed data.

constant mass density and constant magnetic susceptibility. As the comparison between the observed and the calculated profiles is not absolute, the mean values for each type of data along the profile were subtracted from the data before the calculation of the data misfit. No 3-D corrections in the forward calculation were included in this work because the prisms were considered as laterally infinite.

The posterior chain was constructed by applying the Metropolis sampling procedure to the models generated by the prior chain. The joint models generated in this way are, after an initial phase of convergence, representative of the posterior information (prior information plus geophysical data information).

4. Results for the eastern section of the Cadomian belt

Applying the procedure described in Section 3, the prior chain initiated from the model shown in Fig. 1 generated 10^6 prior joint models, two of which are shown in Fig. 3. These models are consistent with the prior information concerning the lithologic field; i.e. lithotypes are fixed at the surface, the number of lithologic regions is preserved, and the volumes and smoothness of the frontiers are comparable for the different lithotypes. The variations of the lithologic models involve the position and shape of the lithologic regions, always attached to their known outcrop at

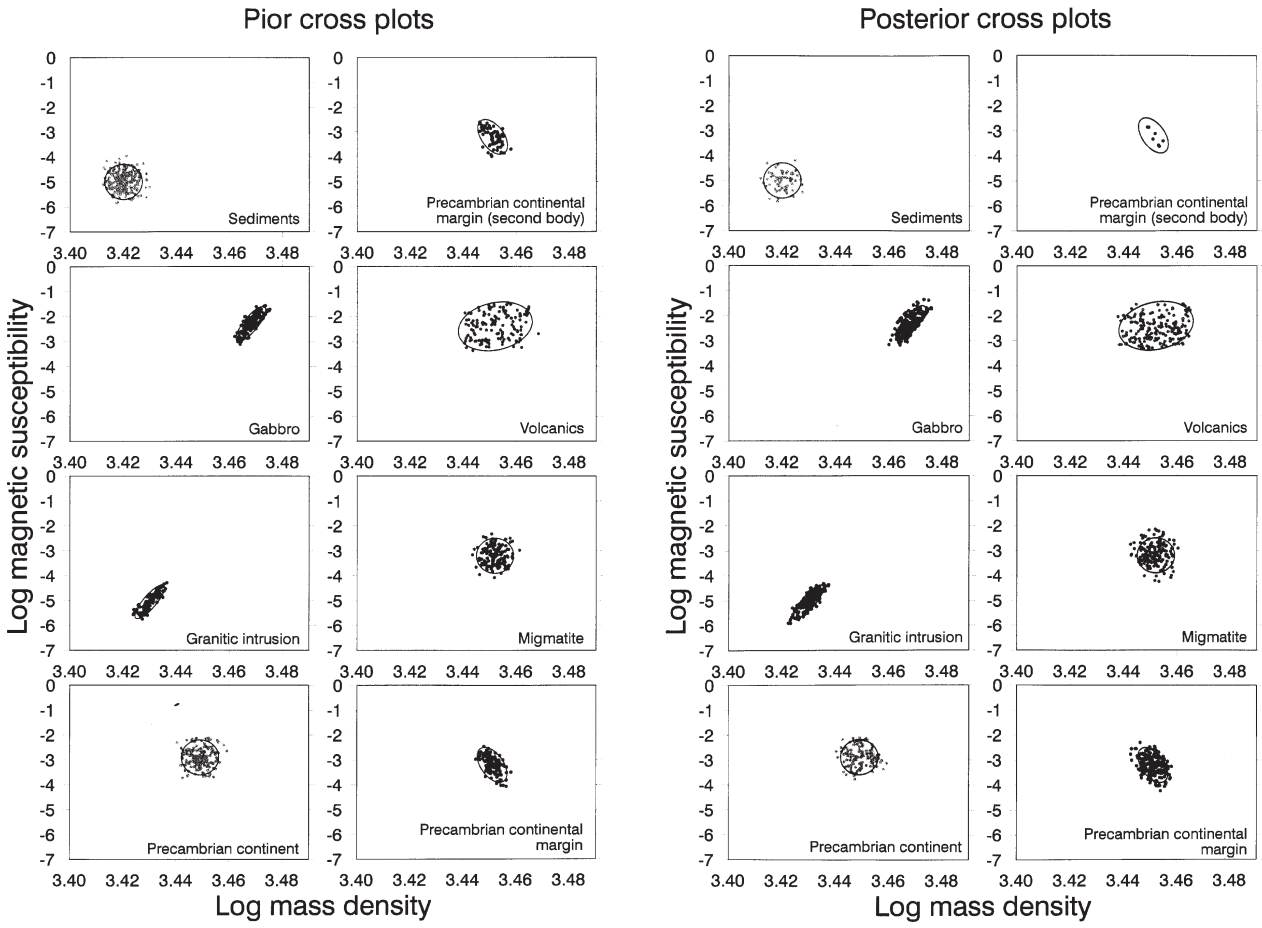

Fig. 4. Cross-plots of the simulated secondary properties for the joint models 300 000 and 800 000 pulled from the chain sampling the prior *pdf* (left) and posterior *pdf* (right) for the Eastern region. The dots correspond to the base 10 logarithms of the mass density and magnetic susceptibility cross-plot in all triangles of the two joint models. The lines show the 2 standard deviation contour of the Gaussian marginal ellipsoid calculated from the prior descriptive parameters given as input for the simulation.

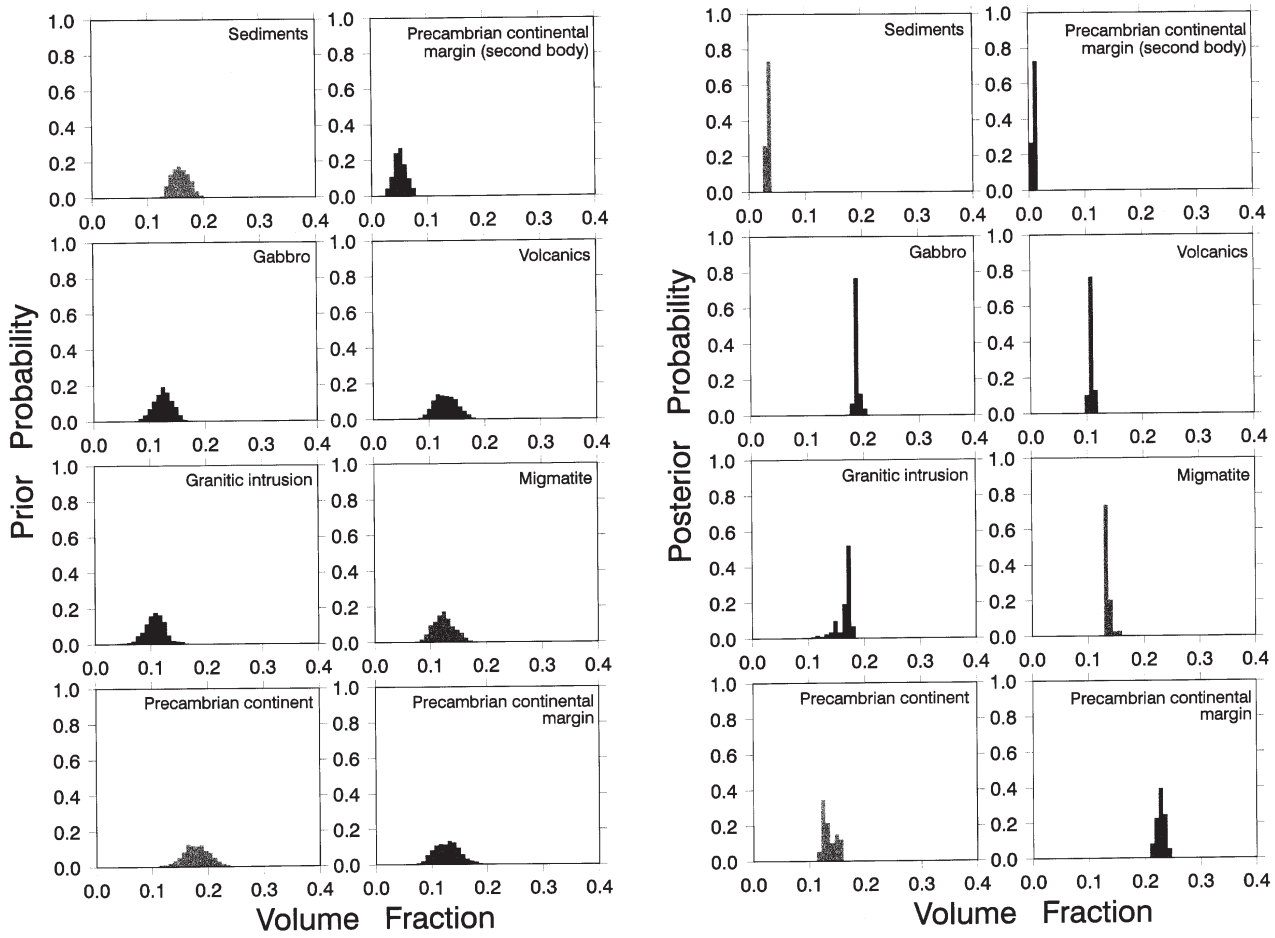

Fig. 5. Histograms of the volume fraction of each lithotype along the chains sampling the prior *pdf* (left) and posterior *pdf* (right) for the Eastern section. Histogram calculation takes into account all lithologic models in the chain between joint model 100 000 and joint model 10^6. The probability is calculated by the frequency of the lithotype at each pixel.

surface. In order to give the model freedom to represent the granite intrusions either outside or inside the Precambrian continental margin, the latter were modelled with two bodies.

The prior information about the secondary properties is also respected; features such as the spatial correlation range are shown, as is the correlation between the mass density and the magnetic susceptibility. Fig. 4 (left) shows cross-plots for the prior secondary properties according to lithology for the two models given in Fig. 3. The points represent simulated properties in the model triangles (monomodal Gaussian model having been used for the simulation of the secondary properties of this chain) and the ellipses indicate the parameters provided to the algorithm as prior information. The cross-plots show good agreement of the simulated properties and the desired global statistics.

Fig. 5 (left) shows the prior histograms of the volume fraction for each lithotype calculated from the lithotype volume fractions in all models between simulation 100 000 and simulation 10^6; the first 100 000 simulations are not used for the histogram calculation to avoid the influence of the initial model configuration.

Fig. 6 (left) shows spatial lithotype histograms of the lithotype frequency in the simulated prior models according to the coordinate position in the 2-D section. Each plot in the figure represents the frequency of a particular lithotype over a fine regular grid of points covering the 2-D section, with the sum of all the plots being equal to unity. This frequency

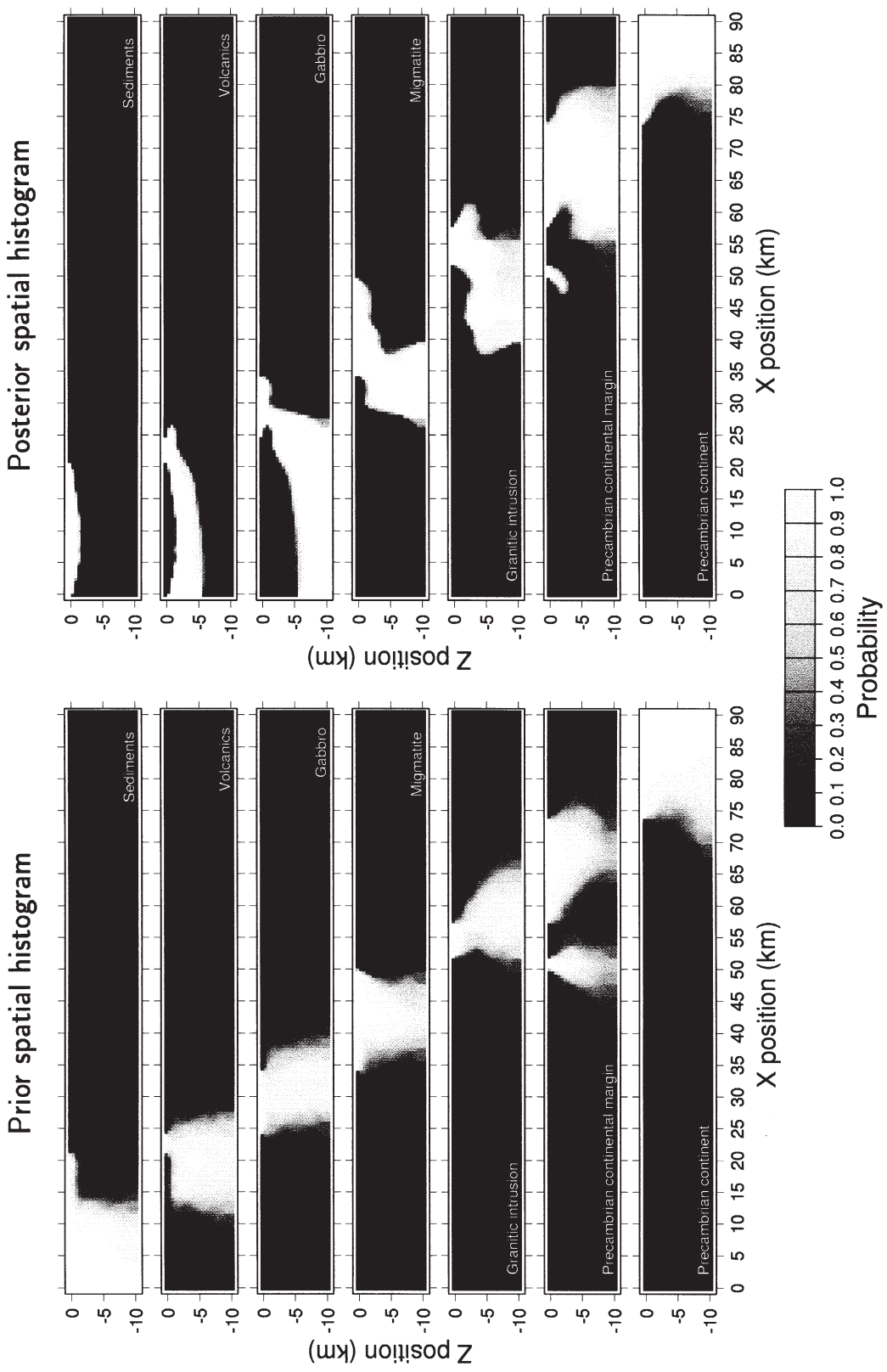

Fig. 6. Lithotype histograms according to position calculated from the chains sampling of the prior *pdf* (left) and posterior *pdf* (right) for the Eastern section. The calculation takes into account all lithologic models in the chain between joint model 100 000 and joint model 10^6. The probability is calculated by the frequency of the lithotype at each pixel.

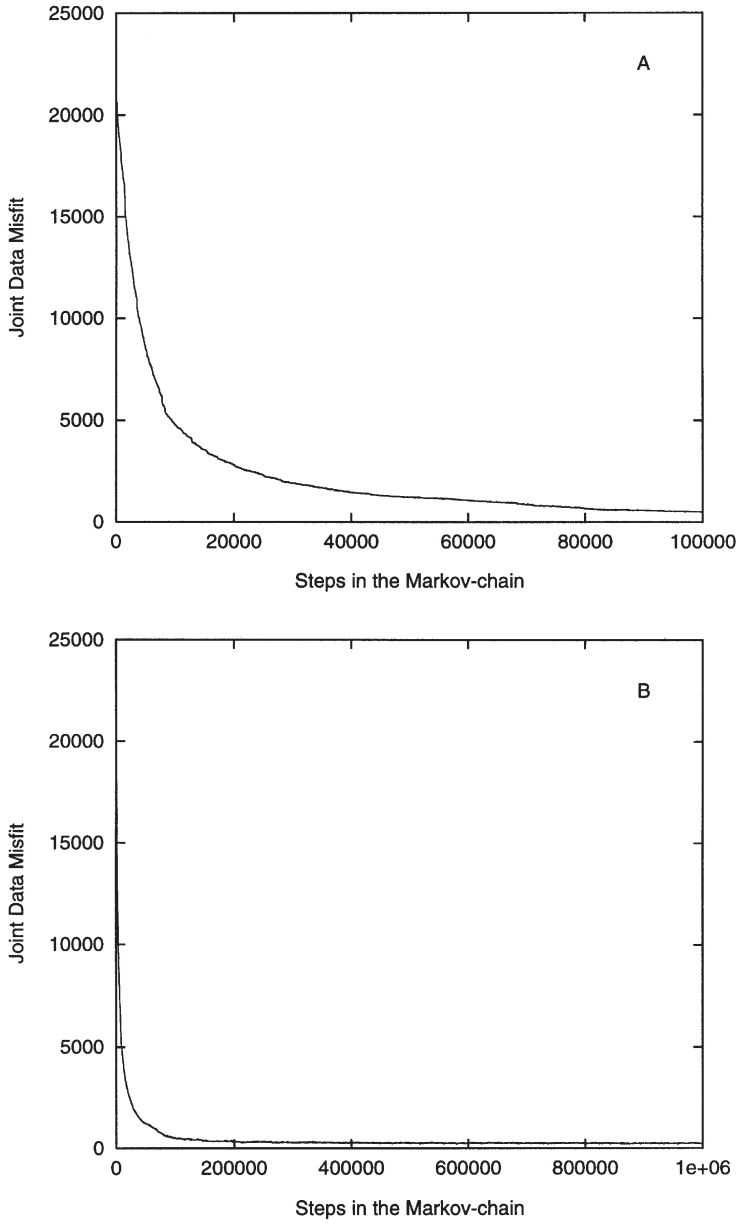

Fig. 7. Joint data misfit along the 10^6 joint model chain sampling the posterior *pdf* for the Eastern section. (A) The first 100 000 iterations; (B) all 10^6 iterations.

represents the estimated prior probabilities for the lithotypes over each grid position. This histogram was also constructed from all the simulated models between model 100 000 and model 10^6.

As seen in the prior lithologic models of Fig. 3 and in the prior lithotype histogram of Fig. 6 (left), the specific shape of the initial model (Fig. 1) is not preserved in the simulated models. This indicates a good variability of the prior chain and is consistent with the ergodicity property of Markov chain samplers that enables them to converge to the sampled distribution with no dependence on the starting model whenever a sufficiently large chain is used.

The posterior chain was performed using the same parameters as for the prior chain, but taking into account the likelihood of the models with the

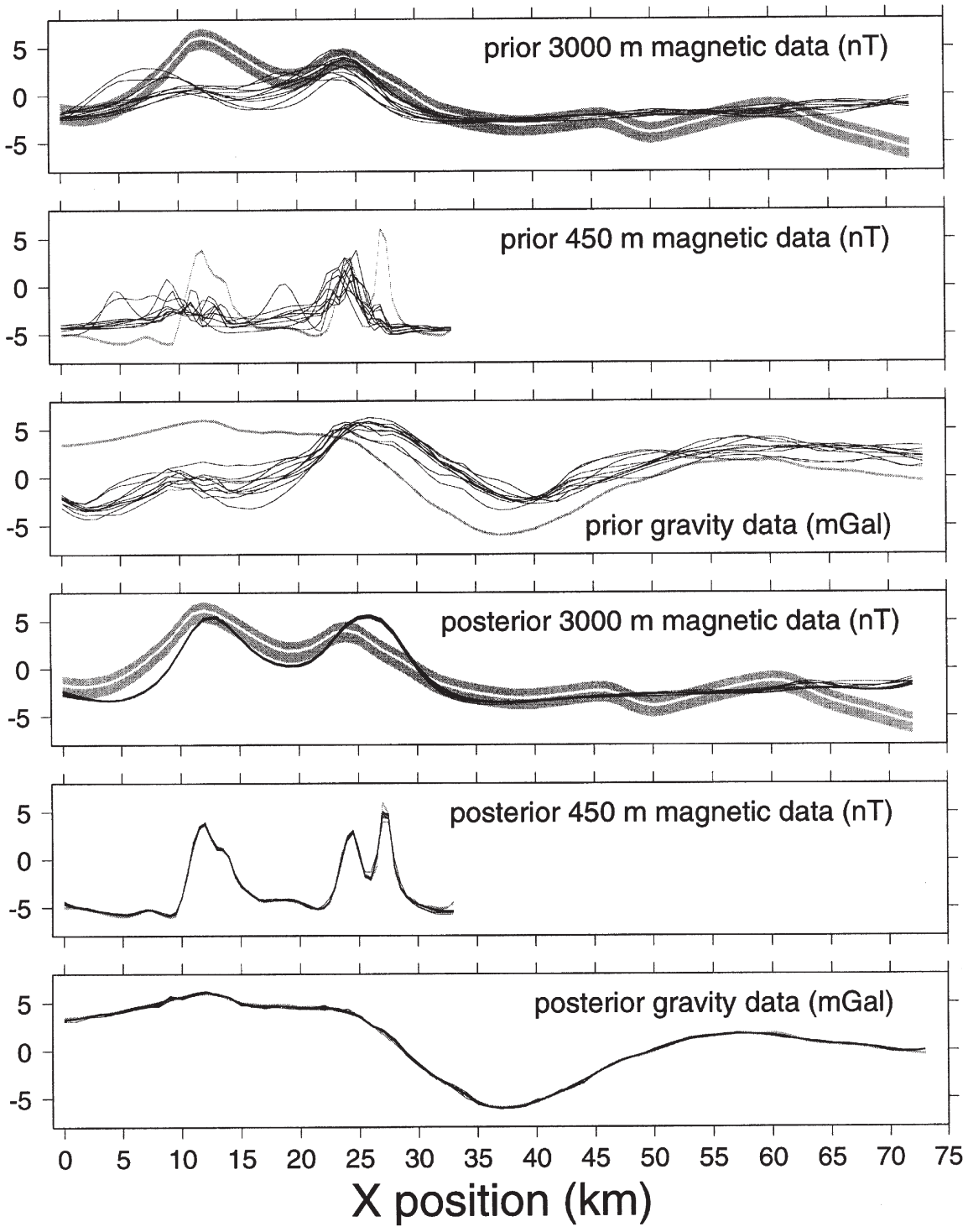

Fig. 8. Calculated data from 10 joint models pulled from the chains sampling the prior *pdf* and posterior *pdf* for the Eastern section. The 10 models were taken from each chain at a regular interval of 100 000 models beginning from model 100 000; hence the models shown in Figs. 3 and 9 are included. Black lines show calculated data; the grey bands are centred in the observed data and indicate ± 1 standard deviation uncertainty of the observations; the observed data is highlighted with a white line for the 3000-m altitude magnetic plots.

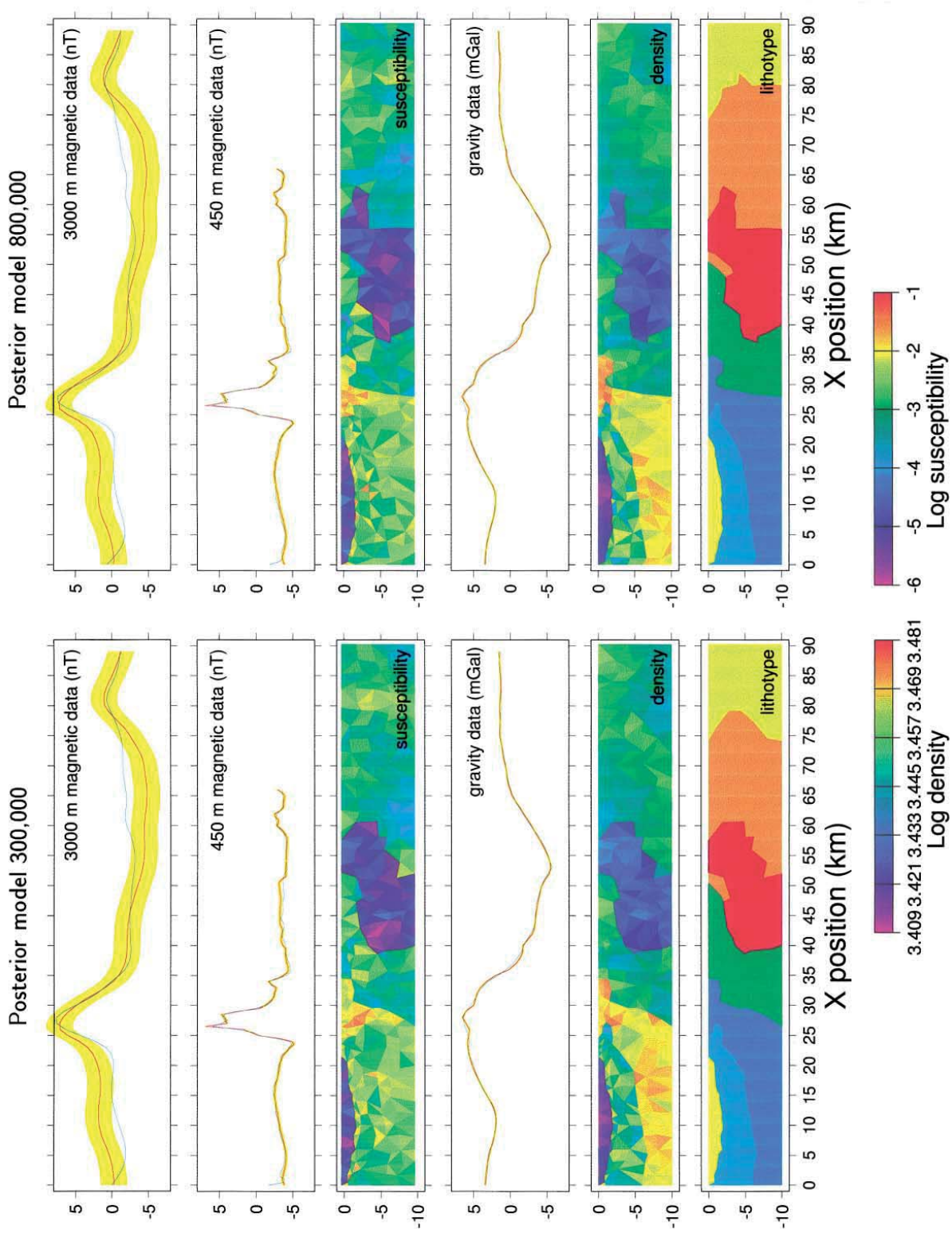

Fig. 9. Joint models 300 000 and 800 000 pulled from the 10^6 joint model chain sampling the posterior *pdf* for the Eastern section. Compare these posterior models with the prior models shown in Fig. 3 (same colour code, scale and units).

observed geophysical data. Fig. 7 shows the progress of misfit reduction during the implementation of the posterior chain for the Eastern section. The plot shows how the data misfits are significantly reduced by the algorithm. The first 100 000 simulations represent a convergence phase, where models are still influenced by the initial model; this phase was excluded from the calculation of the chain statistics, as is usual in Monte Carlo estimation. Simulations 100 000 to 10^6 represent the sampling phase.

The calculated data for 10 joint models pulled from both the prior and the posterior chains are given in Fig. 8, which shows the variability of the data calculated from the models of the prior chain contrasted with the data calculated from the models of the posterior chain—the latter are constrained to follow the observations according the joint geophysical likelihood function (8). It also shows that the joint models generated by the posterior chain adequately explain the data. The 3000-m-altitude magnetic data and the 450-m-altitude magnetic data are not completely consistent as they represent information from different surveys; the higher resolution 450-m-altitude magnetic data are characterized by a much smaller relative uncertainty than the 3000-m-altitude magnetic data, as expected.

Fig. 9 shows two joint models pulled from the 10^6 posterior joint model chain along with both the calculated geophysical data from these models and the observed geophysical data. It is seen that the calculated data are very proximate to the observed data and that they also respect the features of the prior information such as the fixed lithotypes at the surface, the topology and the petrophysical and geostatistical descriptions (correlation between mass density and magnetic susceptibility, correlation range, etc.).

The same monomodal Gaussian model as for the prior chain was used for the property description of the posterior chain. The corresponding cross-plots (Fig. 4 (right)) show that the secondary property priors were in general preserved in the posterior chain, tolerating some small changes such as the tendency of the volcanics toward a lower mean magnetic susceptibility.

Posterior histograms of the volume fraction for the lithotypes are shown in Fig. 5 (right). Comparison with the prior histograms (Fig. 5 (left)) shows that the expected values for the volume fraction of each lithotype are remarkably constrained by the geophysical data, resulting in a much smaller dispersion of the posterior histograms. In addition, it is seen that the centres of the histograms vary significantly for some lithotypes after incorporating the geophysical information. The figure also shows the smaller estimated volume for the sediments and the larger estimated volume for the granitic intrusion.

In the posterior spatial histograms of the lithotypes (Fig. 6 (right)), we once again see that the spatial organization of the lithotype regions is much better constrained and significantly different than in the prior chain, which indicates that the geophysical data is introducing significant information to the posterior *pdf* concerning the geometrical organization of the lithotype regions.

As seen from the posterior joint models (Fig. 9) and the posterior lithotype histograms (Fig. 5 (right)), the gravity negative anomaly is largely explained by the geometry of the granite which dips to the north and occupies a larger volume than the expected prior volume fraction or the volume represented in the initial model. The gravity positive anomaly is mainly explained by the geometrical structure of the gabbro and volcanics that also dip to the north. This configuration may be consistent with the geological model of an oblique obduction of the volcanic arc system over the continental domain. The geometry of the boundaries is not as smooth as was conceived in the preliminary model for the region (Fig. 1) and shows some significant deformation at the nappe front that could be associated with the Cadomian or Variscan tectonism. The shape of the gabbro near the surface may be explained by a flower-type structure, common in fault zones under a transpressive-stress regime.

We repeated the posterior chain for the Eastern section using different random number sequences and obtained similar results. We also applied multimodal simulation of the secondary properties to the gabbro and volcanics; again, the general results do not differ significantly from the results obtained with the monomodal simulation.

5. Results for the Western section of the Cadomian belt

A model pulled from the posterior chain of the

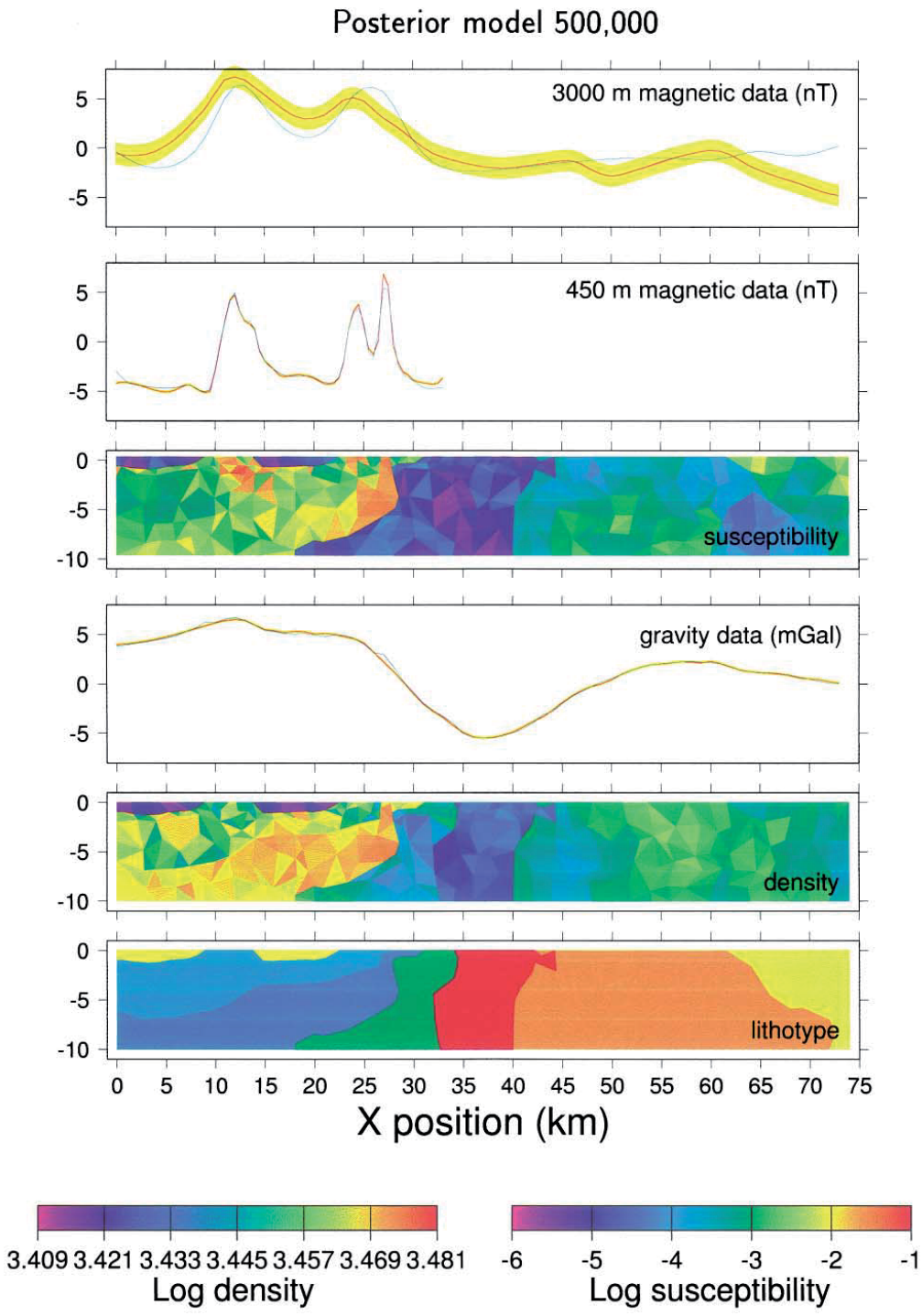

Fig. 10. Joint model 500 000 pulled from the 10^6 joint model chain sampling the posterior *pdf* for the Western section, using a monomodal simulation of the secondary properties. Colour code, scale and unit are the same as in Fig. 3.

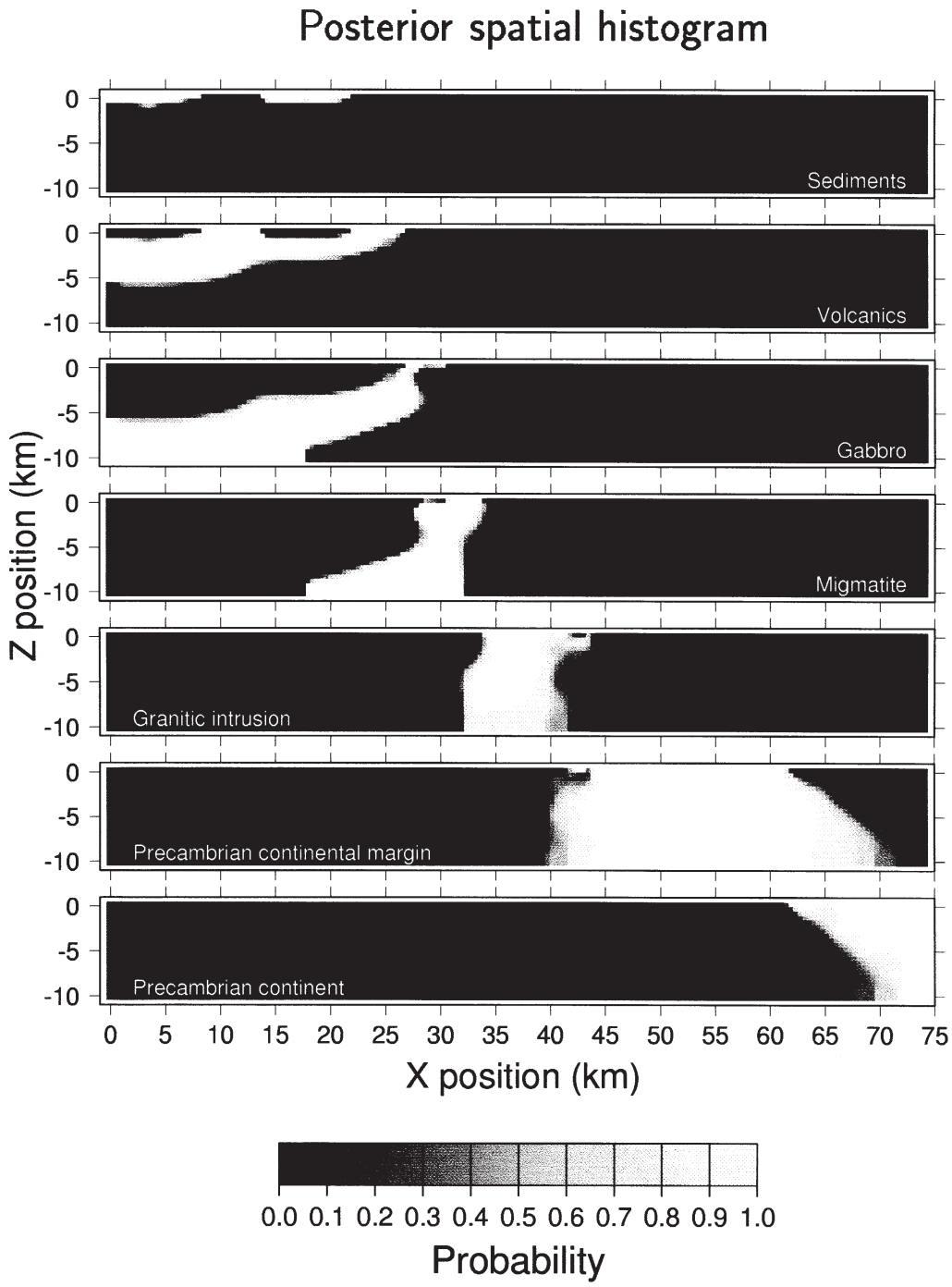

Fig. 11. Lithotype histogram according to position calculated from the chain sampling the posterior *pdf* for the Western section with a monomodal simulation of the secondary properties. The calculation takes into account all lithologic models in the chain between joint model 100 000 and joint model $10^{6.}$ The probability is calculated by the frequency of the lithotype at each pixel.

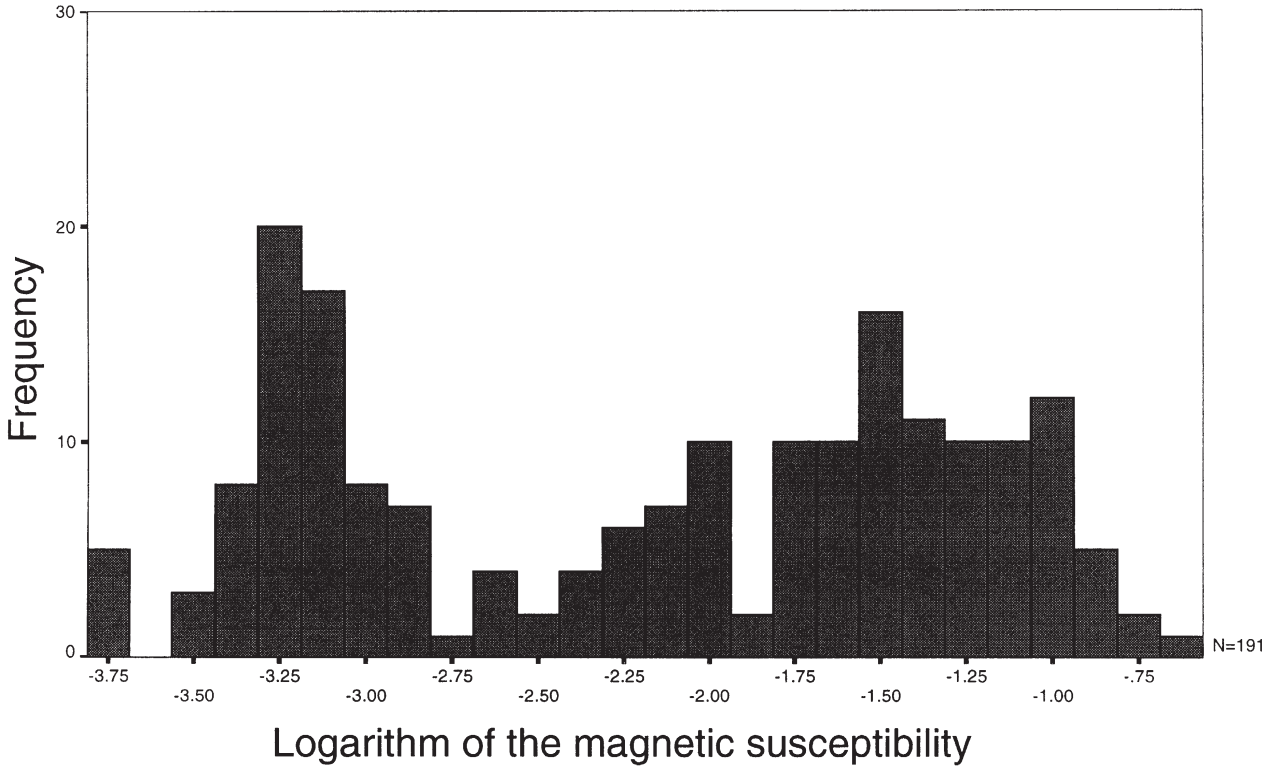

Fig. 12. Histogram of the base 10 logarithm of the magnetic susceptibility (in SI units) from the available field rock samples collected within the

Western section processed using a monomodal simulation of the secondary properties reveals a probable discontinuous deep structure along the Main Cadomian Thrust, at the contact between the volcanic arc system and continental domain. This agrees well with the explanation of the high-resolution magnetic anomalies (450-m altitude; see Fig. 10, at horizontal position between 23 and 28 km) which require both a shallow (1–2 km depth) and a deep (2–5 km depth) contribution of a highly magnetized gabbro.

The structure is significantly stable along the posterior chain and can be identified in the spatial lithotype histograms shown in Fig. 11. It was nevertheless decided to study the reliability of this structure through a multimodal simulation to represent the secondary properties in view of the fact that the original statistical analysis of the secondary properties for the gabbro and volcanics showed a multimodal distribution, which is particularly evident from the magnetic susceptibility. Modelling this type of distribution with a monomodal Gaussian simulation, moreover, could be artificially smoothing the magnetic susceptibility field and have consequences on the lithologic image estimation. Hence a multimodal type of simulation was performed to reproduce in the model the realistic contrasts of the property.

Fig. 12 gives a histogram of the magnetic susceptibilities of field samples within the volcanic arc system as measured in the laboratory (Cauvin-Cayet et al., 2001). It shows two major modes in the distribution of the magnetic susceptibility that would appear to characterize the volcanics, since they are present in varied proportions in all samples. Joint representation of the secondary properties by cross-plots of mass density and magnetic susceptibility suggested, although the data was scarce, a description of the secondary properties by 2 and 4 modes in the gabbro and volcanics, respectively. In any case, this description was more accurate than the monomodal description adopted in the simulations already shown.

A joint model pulled from the prior chain generated for the Western section using the multimodal simulation of secondary properties is given in Fig. 13 (left). As in the Eastern section, the prior information was

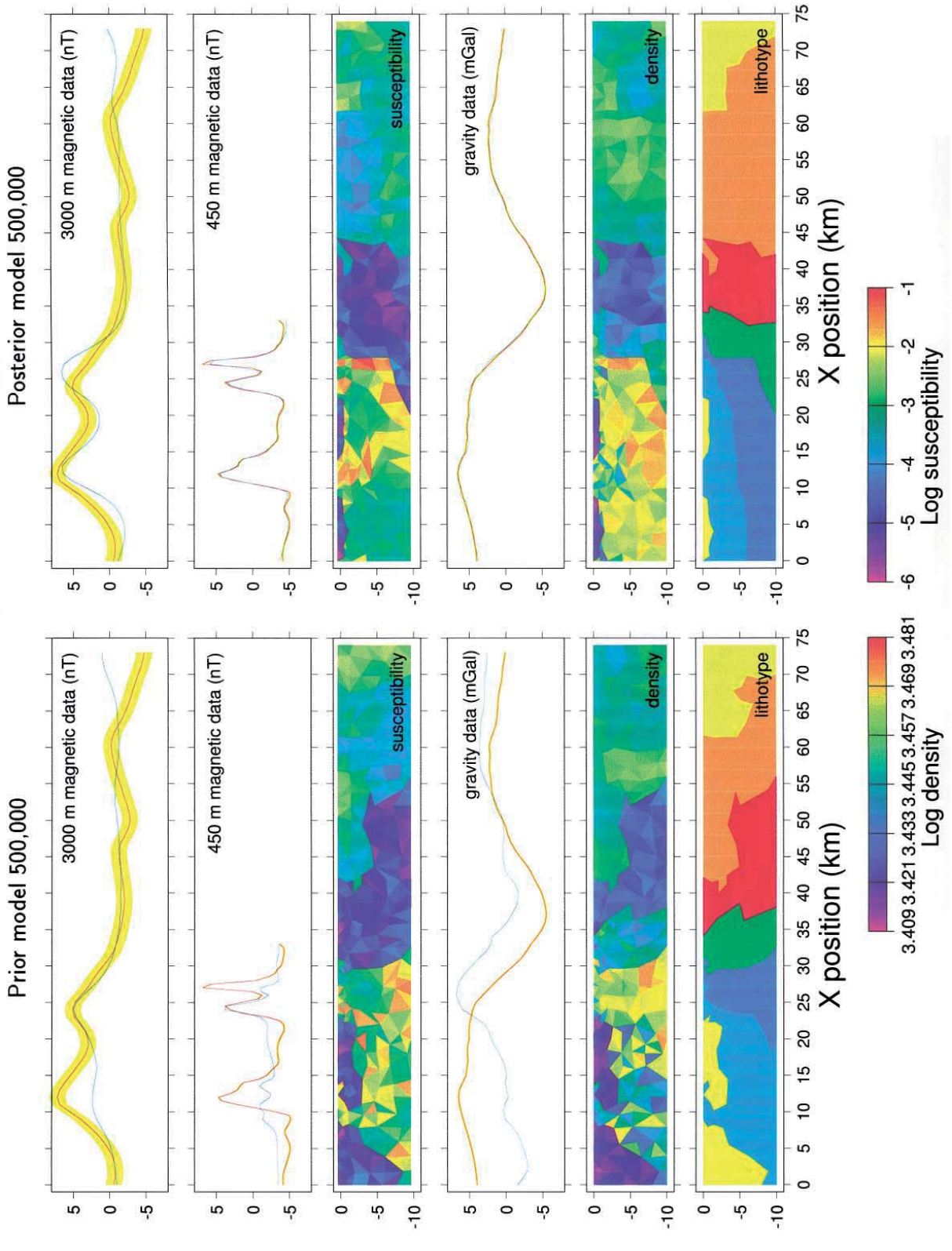

Fig. 13. Joint model 500 000 pulled from the 10^6 joint model chains sampling the prior *pdf* (left) and the posterior *pdf* (right) for the Western section. The simulation of the secondary properties within the gabbro and volcanics was multimodal. Colour codes, scales and units are the same as in Fig. 3.

respected by the prior models maintaining a good variability on the shape of the lithotype regions. Fig. 14 (left) shows the prior cross-plots of the secondary properties according to lithology for the simulation using a multimodal model for gabbro (2 modes) and volcanics (4 modes) and a monomodal model for the rest of the lithotypes. It also shows the consistence between the parameters provided as prior information to the modelling algorithm and the actual simulated properties. Prior volume and lithotype histograms are given in Figs. 15 (left) and 16 (left).

The posterior chain with the multimodal secondary simulation was performed with the same parameters, but respecting the likelihood with the observed geophysical data. The joint data misfit progress along the posterior chain is shown in Fig. 17, and a joint model pulled from the posterior chain is given in Fig. 13 (right). As in the Eastern section, the gravity negative anomaly is mostly explained by the geometry of the granitic intrusion, which is deeper than its representation in the preliminary model of the region (Fig. 1). The gravity positive anomaly in the north is explained by the geometry of the gabbro and volcanics. The 450-m-altitude magnetic data exhibit two positive anomalies explained by zones of high magnetization in the gabbro and volcanics with the southernmost anomaly located very near the border of the outcrop. This anomaly is integrated by an envelope with a base of 10 km and two smaller oscillations; the

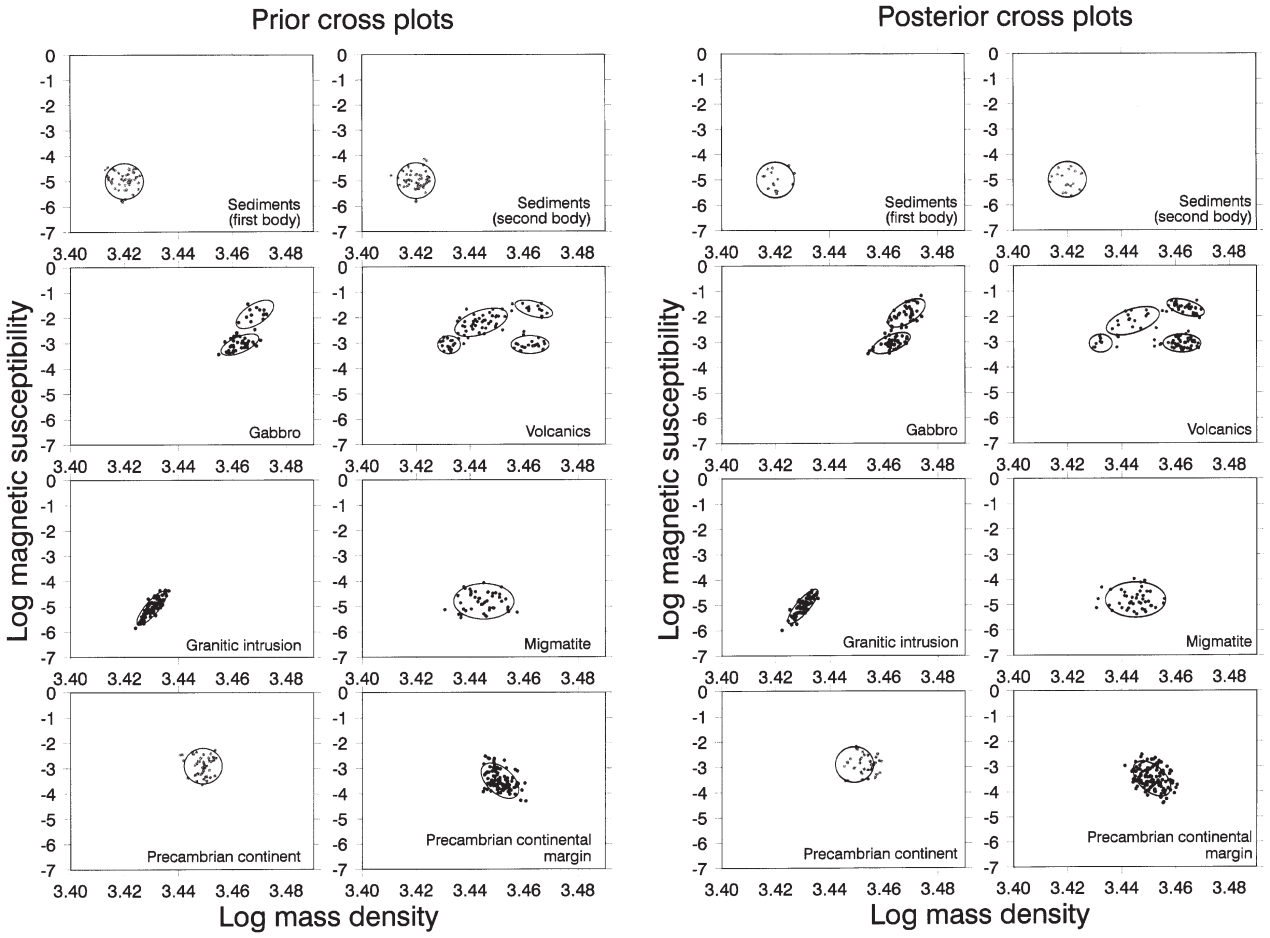

Fig. 14. Cross-plots of the simulated secondary properties for the joint model 500 000 pulled from the chains sampling the prior *pdf* (left) and the posterior *pdf* (right) for the Western section. The simulation of secondary properties followed a multimodal (mixed Gaussian) model. The lines show the two standard deviation contour of the Gaussian marginal ellipsoid for each mode, calculated from the descriptive parameters given as input for the simulation. Other symbols and units are the same as in Fig. 4.

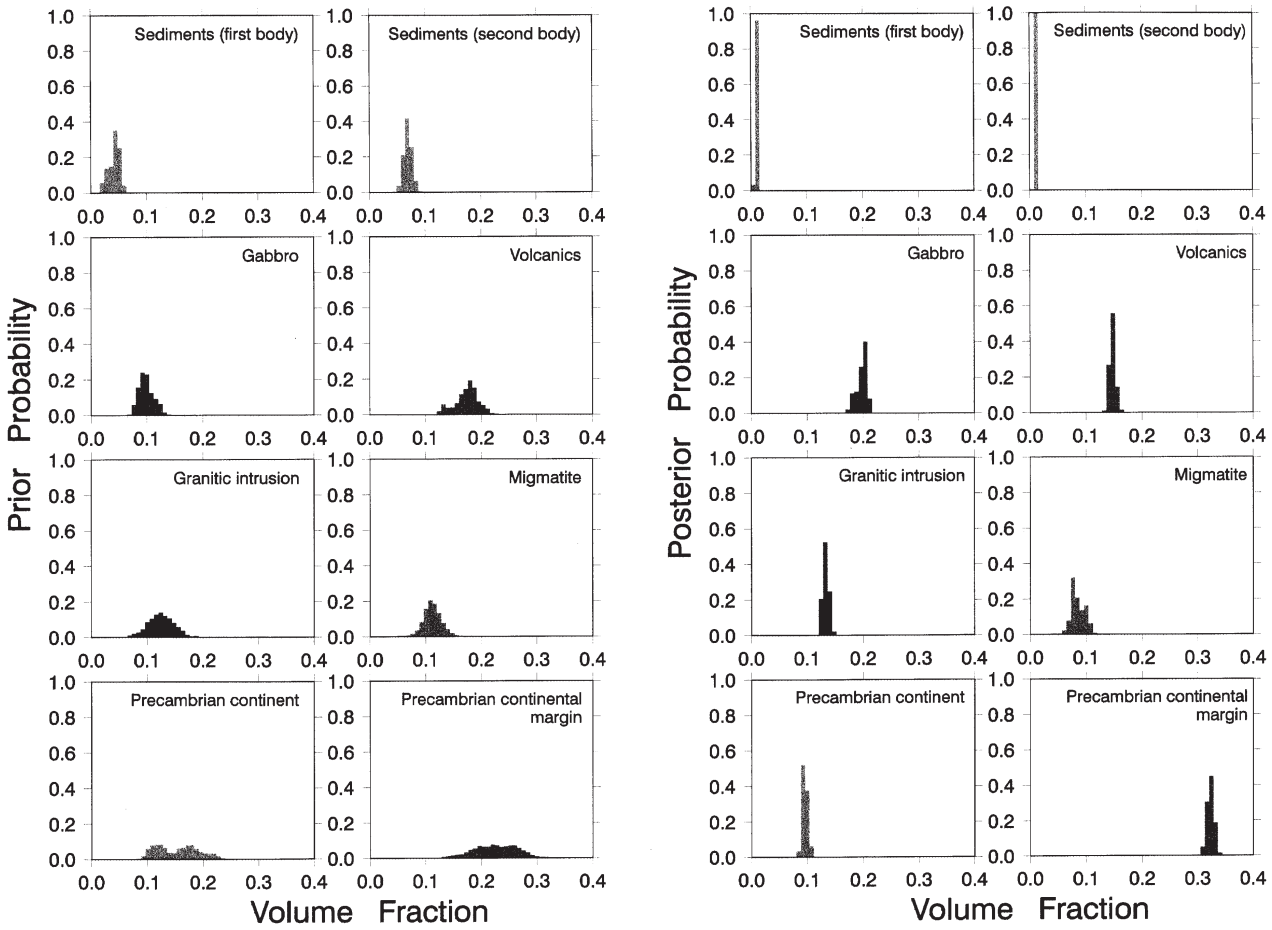

Fig. 15. Histograms of the volume fraction of each lithotype along the chains sampling the prior *pdf* (left) and posterior *pdf* (right) for the Western section. Histogram calculation takes into account all lithologic models in the chain between joint model 100 000 and joint model 10^6. The probability is calculated by the frequency of the lithotype at each pixel.

larger wavelength feature is explained in the magnetic susceptibility model by a high magnetic susceptibility zone in the gabbro at a depth between 3 and 7 km, whereas two shallower magnetized zones (in gabbro and volcanics) contribute to the two local maxima of shorter wavelength.

Fig. 14 (right) shows the posterior cross-plots of the secondary properties. As in the Eastern section, the prior information on the global statistics of the secondary properties was in general maintained in the posterior models, tolerating some small adjustments. As can be seen from comparing the prior and posterior cross-plots, the posterior model has changed the proportions among the modes of the volcanics, with an increased representation of the two modes with higher density. In addition, the centroids for the Precambrian continent and Precambrian continental margin show small deviations toward higher density values. Figs. 15 (right) and 18, respectively, show the posterior volume fraction of the lithotypes, significantly constrained by the geophysical data, and the calculated data for 10 joint models pulled at regular intervals from the prior and posterior chains with multimodal simulation of the secondary properties.

Fig. 16 (right) presents the lithotype histogram for the posterior chain, which shows a vertical boundary for the volcanic arc system (3–6 km depth boundary between the gabbro and migmatite) inferred from the

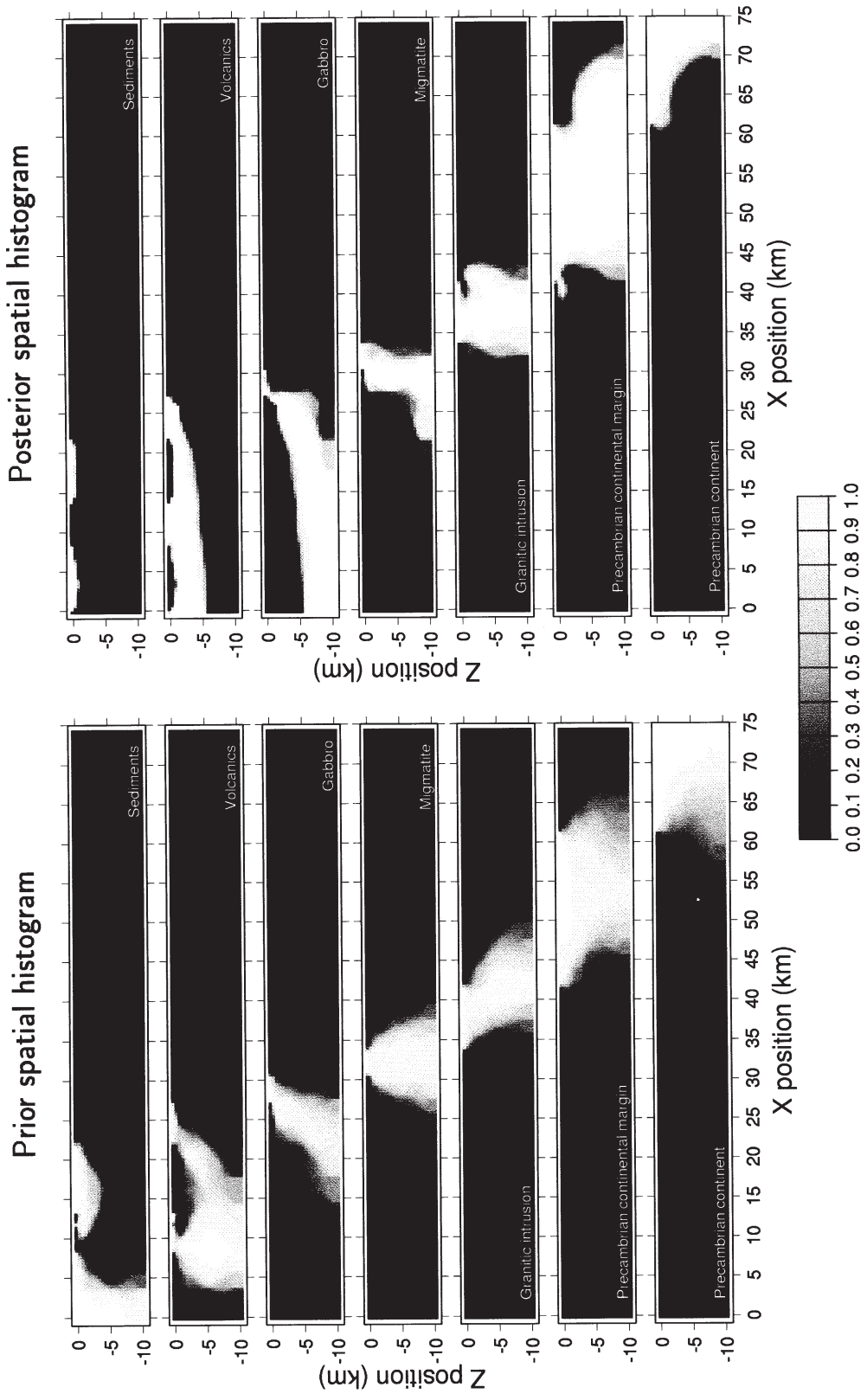

Fig. 16. Lithotype histograms according to position calculated from the chains sampling the prior *pdf* (left) and the posterior *pdf* (right) for the Western section. The calculation takes into account all lithologic models in the chain between joint model 100 000 and joint model 10^6. The probability is calculated by the frequency of the lithotype at each pixel.

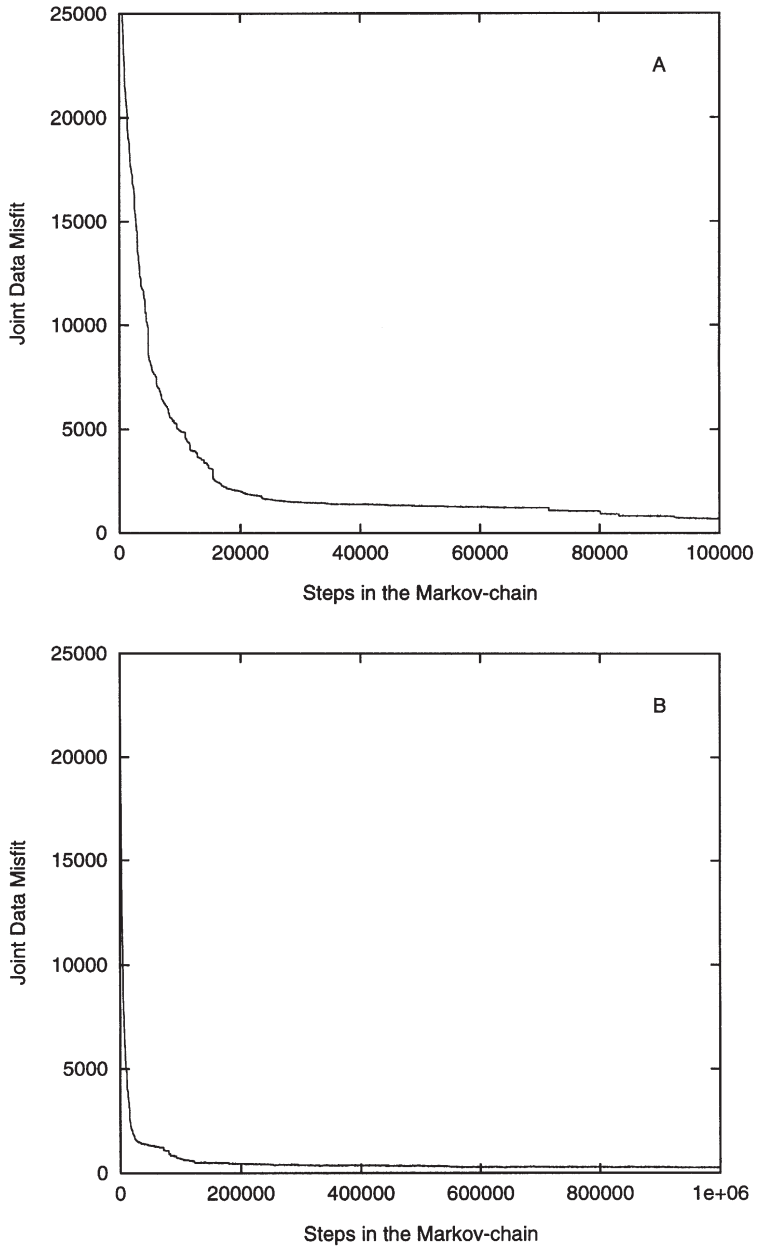

Fig. 17. Joint data misfit along the 10^6 joint model chain sampling the posterior *pdf* for the Western section, with a multimodal simulation of the secondary properties. (A) The first 100 000 iterations; (B) all 10^6 iterations.

geophysical data. The posterior chain, with its more accurate multimodal simulation of the secondary properties for the gabbro and volcanics, also shows the discontinuous structure previously defined by the monomodal Gaussian model for the secondary properties.

6. Discussion on the lithologic tomography results for the Cadomian belt

The overall architecture of the studied area of the Cadomian belt is discussed in relation to the joint models generated by the posterior chain. The statistical

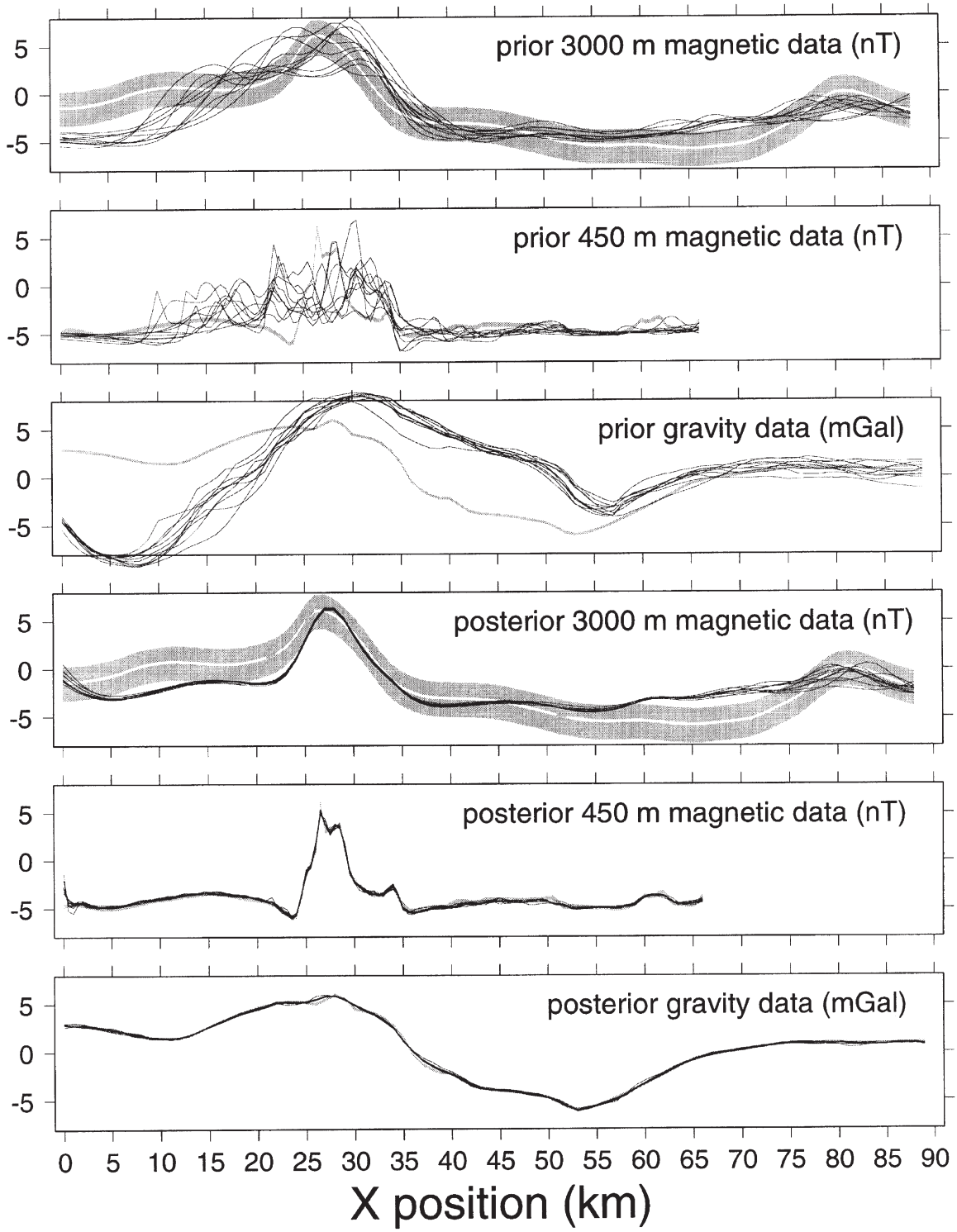

Fig. 18. Calculated data from 10 joint models pulled from the chain sampling the prior *pdf* and posterior *pdf* for the Western section. In both cases, multimodal simulation of the secondary properties was used within the gabbro and volcanics. The 10 models were taken from each chain at a regular interval of 100 000 models beginning from model 100 000. Black lines show calculated data; the grey bands are centred in the observed data and indicate ± 1 standard deviation uncertainty of the observations; the observed data is highlighted with a white line for the 3000-m altitude magnetic plots.

tomographic images showing a vertical segment (Fig. 16) or a steeply southward-dipping segment (Fig. 11) in the Western section of the belt may be explained in different ways. In the context of the Cadomian orogeny, the discontinuity at the front of the volcanic arc system may correspond to reverse faulting resulting from continued compressional stress after the collision. As all the Cadomian belt models recognize, to a greater (Treloar and Strachan, 1990) or lesser (Brun and Balé, 1990) extent, the role of lateral displacements, the presence of vertical strike-slip faults between nappes or flower-type structures should be expected.

An alternative explanation could also be considered in the context of the Variscides. Edel and Weber (1995), on the basis of geophysical and geological evidence, presented an interpretation of the present location of Cadomian terranes at the scale of Western Europe. According to their model, the Cadomian belt of northern Brittany can be correlated with remnants of similar belts within the Saxothuringian and Bohemian regions, and was originally part of a much larger and fairly continuous belt that was sectioned and separated by large-scale dextral shearing during the Variscan, with displacements of the order of hundreds of kilometres.

The Eastern section is coincident with a seismic profile shot in 1995 and interpreted by Bitri et al. (1997, 2001) who considered that the Port Morvan Fault, the Main Cadomian Thrust and the Plouer–Cancale Fault dip, respectively, to the south, north and north. This general interpretation is confirmed by the models pulled from the posterior chain for the Eastern section (Fig. 9) and the histogram of lithotype frequency (Fig. 6), except that the shape of the Main Cadomian Thrust deviates from a plane feature. The particular shape obtained for this contact with the posterior chain explains a small, but significant, secondary peak of the 450-m altitude magnetic anomaly located above the fault zone (see position 34 km of the magnetic data and the magnetic susceptibility model of Figs. 8 and 9). Finally, the tomographic images of the granite intrusions showed that the massifs are rooted at more than 10 km depth and have an important volume fraction; the geometry suggests that the intrusion followed the Plouer–Cancale Fault zone.

The posterior chain is also informative about the secondary parameters. The magnetic susceptibility posterior models of Fig. 13 and the histogram of lithotype frequency of Fig. 16 indicate that the regions of high magnetic susceptibility in the Saint-Brieuc Unit of the Western section are probably located near the Main Cadomian Thrust. The genesis of a larger concentration of magnetic minerals in such zones could be stimulated by hydrothermal alteration, as it has been shown that magnetization can be associated with the serpentinization of peridotite (Horen, 1997). About 15 km to the north of this contact (see position 12 km of the magnetic susceptibility model of Fig. 13) a second zone of high magnetization seems to be related to the gabbrodiorite intrusion, which can also be a source of magnetization.

Another feature from the posterior information on the secondary properties concerns the spatial variability of the properties, in particular for the volcanics. This was the most heterogeneous lithotype considered in the model and the analysis of field samples showed significant dispersion in the secondary properties and significant variation across neighbouring site sample locations. A short range of spatial correlation (0.5 km) was used in the modelling to allow a significant spatial variability of the magnetic susceptibility and mass density between neighbouring triangles. The posterior models of the magnetic susceptibility (Figs. 9, 10 and 13) show that a significant spatial correlation within a larger range of 3 or 4 km exists for both gabbro and volcanics. It also shows that the spatial correlation in highly magnetized regions is not particularly affected by the boundaries between these lithologies. This indirect evidence, as well as the similar bimodal behaviour of the magnetic susceptibility, suggests that the high magnetization mode of these rocks may obey common environmental genetic factors that affected the volcanic arc system.

The results obtained have to be considered as preliminary because the method should be applied to more sections crossing the region for a more representative spatial image of the volume under study, especially if implemented in 3-D. Equally, the acquisition of additional petrophysical field data could contribute to a more accurate statistical description of the secondary properties.

In the method described here, the detailed characterization of media properties, in particular their dependence on lithology, their correlation and their

spatial behaviour, is fundamental and has a direct influence on the tomographic images of the lithotype geometry. The application of the method should be accompanied by a specially dedicated campaign to fully address the description of the properties.

In the Cadomian belt study, field data were available for the north of the area and the global statistics for the lithotypes were well constrained. The parameters describing the statistics of the secondary properties without direct field data support were obtained from conventional petrophysical tables or from data from other regions. Some small variations changing the description of the secondary properties were tested, particularly for the lithotypes in the south of the area. As expected, these variations affected the inferred geometry, but did not change the major features highlighted in the discussion and the results.

As mentioned, the Precambrian continental margin of the Fougères Unit and the Precambrian continent of the Central Armorican Domain have a very similar signature in the observed gravity and magnetic data and for the secondary properties. Thus, although a major tectonic lineament is suspected, the shape of the contact between these two units is not significantly constrained by the data and should not be taken into account for interpretation.

Although, in the present application, we interpolated the observed data at regularly spaced intervals along the section profiles, it should be mentioned that the method can also be used with irregularly spaced station positions. For a 3-D implementation of the method, the true station positions and the original station data would most likely be used, rather than interpolated data over a grid of points. In the same way, the triangulation of the section can be irregular to enhance the model spatial resolution in specific zones. For the Cadomian belt, as shown in Fig. 1, we used a finer triangulation near the surface for the northern area of the model. This enhanced spatial resolution was introduced in the model to better explain the 450-m altitude magnetic data.

For the construction of the Markov chain samplers we adopted a Gaussian model for the observed data uncertainties and two different types of models for the conditional *pdf* of the secondary parameters. The generation of the primary Markov chain was based on marginal and conditional *pdf* on individual model parameters, as well as on some global parameters. The method is not attached to a particular choice in the form of the *pdf* and can be implemented with any type of *pdf* in the different components of expression (1). Future developments of the method are envisaged in two directions: a generalization to 3-D and the incorporation of other types of geophysical data. A 3-D representation of the lithotypes could be achieved by performing the 2-D inference along several sections accompanied by lateral interpolation of the statistics to generate posterior 3-D spatial lithotype histograms enabling, for instance, lithotype spatial probabilities to be mapped in horizontal charts at different depths. A full 3-D implementation of the method would be, however, much more advantageous to truly represent: (a) 3-D effects in the data; (b) station densities at the surface; and (c) the constraints on the shape of lithologic regions arising from the 3-D continuity in bounding frontiers and 3-D topology.

The method allows the incorporation of additional types of information, such as testing the mechanical stability of the proposed mass density distributions or constraining the models with seismic or electromagnetic observations. The information could be included in the likelihood function and incorporated into the sampling algorithm, assuming that the forward problem could be solved in a relatively efficient computational way.

7. Summary and conclusions

The new method that we have presented, for inferring the subsurface organization of the major lithotypes present in a region from geophysical observations and prior information about the geology and petrophysical characterization of the rocks, is conceived to integrate the large amount of diverse data generated by multidisciplinary survey and exploration programmes and provide a general probabilistic description of the posterior joint property fields.

The method demands the joint representation of several properties characterizing the media and the definition of the available information in terms of *pdf* defined over the model parameter space. The prior information about the relationships between the media properties introduces significant constraints in the joint models and couples the inversion of the

different available geophysical datasets. The posterior information is obtained using specialized algorithms, i.e. Markov chain samplers, to generate joint models from the posterior *pdf* and calculate posterior probabilities from a large collection of the sampled joint models.

The sampling chain architecture follows the structure of the posterior *pdf* in expression (1). A primary chain is constructed to generate lithologic models that present good variability in their characteristics and respect the prior information constraints. Lithologic models generated in this way are provided with secondary property fields according to the conditional *pdf*, thus constructing a chain sampling joint models from the prior *pdf*. The joint model outcomes from the prior chain are analysed, as are its statistics, to verify that they followed the desired prior information. Finally, the posterior chain is constructed taking into account the information provided by the likelihood with the geophysical observations.

Preliminary results on the application of this method to the Cadomian belt of northern Brittany have provided valuable information through combining the different types of geophysical data together with the constraints of the prior information. The 2-D tomographic images of spatial lithotype probabilities show a deformed structure of the volcanic arc system, suggesting significant deformation and faulting of the original obducted crust. These features are within the geological expectations due to the strong Cadomian and Variscan tectonism that configured the present structure of the region.

The probable 2-D configuration of the granitic intrusions, according to the available data and prior information, shows a deep-rooting of the intrusions with a volume fraction at least as representative as the exposed area at the surface. The intrusions are inclined approximately parallel to the direction of the boundary between the obducted volcanic arc and the continental margin, suggesting that the ascent of the granite followed an inherited zone of weakness in the crust.

As regards the organization of multidisciplinary surveys and exploration programmes, if the application of this method is to be envisaged, some changes in the conventional procedure would be necessary. Notably, the petrophysical and geostatistical characterization of the major lithologic domains should be strengthened, as this is an important component of the posterior *pdf* in expression (2), and should possibly be preliminary to the acquisition of new geophysical data. The modelling of the geophysical fields, based on realistic descriptions of the media properties, could help in the decisional process defining the methods and geometry for the geophysical acquisition.

Acknowledgements

The theory described in this work was developed with the collaboration of Albert Tarantola (IPGP) through frequent significant discussions. The authors are indebted to their many colleagues who interacted with them during this research, and in particular to Cathy Truffert (BRGM) and Pol Guennoc (BRGM) who provided the geophysical, geological and petrophysical datasets used in this work and who also helped with the discussion of the geology in the initial stage of the project — our thanks to all of them. The authors also wish to acknowledge the recommendations made by the referees E. Burov and M. Daignières. This work was funded by the GeoFrance 3-D project and the CDCH of the Universidad Central de Venezuela. GeoFrance 3-D Publication 36.

Appendix. The Metropolis sampler

The Metropolis sampler is a general purpose method for sampling from any factored *pdf*, $\pi(\mathbf{x}) = c\rho(\mathbf{x})L(\mathbf{x})$ with $\rho(\mathbf{x})$ being a prior *pdf*, $L(\mathbf{x})$ a likelihood function, c a normalization constant and $\pi(\mathbf{x})$ a posterior *pdf*. The algorithm can be briefly enunciated as follows. Considering that the chain is currently in the step t with an outcome $\mathbf{x}^t$, the next outcome $\mathbf{x}^{t+1}$ is determined according to the following rule:

- Consider $\mathbf{x}^t$ to be the current model in a prior chain (i.e. ergodic to $\rho(\mathbf{x})$) and generate a candidate $\mathbf{x}_{\text{can}}^{t+1}$ outcome from the prior chain.
- Make $\boldsymbol{x}^{t+1} = \mathbf{x}_{\text{can}}^{t+1}$ with probability

$$p = \min[1, L(\mathbf{x}_{\text{can}}^{t+1})/L(\mathbf{x}^t)] \tag{A1}$$

- Otherwise, make $\mathbf{x}^{t+1} = \mathbf{x}^t$
- Continue with Eq. (A1).

The Markov chain defined in this way is ergodic to $\pi(\mathbf{x})$. A detailed description and discussion on the Metropolis sampler can be found in the work of Hastings (1970), Tierney (1994) and Mosegaard and Tarantola (1995).

References

Besag, J., Green, P., Higdon, D., Mengersen, K., 1995. Bayesian computation and stochastic systems. Stat. Sci. 10, 3–66.

Bitri, A., Brun, J.P., Chantraine, J., Guennoc, P., Marquis, G., Marthelot, J.M., Perrin, J., Pivot, F., Tournerie, B., Truffert, C., 1997. Structure crustale du bloc cadomien de Bretagne Nord (France): sismique réflexion verticale et sondage magnétotellurique (projet Géofrance 3-D—Armor). C. R. Acad. Sci. Paris 325, 171–177.

Bitri, A., Brun, J.P., Truffert, C., Guennoc, P., 2001. Deep seismic imaging of the Cadomian thrust wedge of Northern Brittany. Tectonophysics 331 (1–2), 65–80.

Bosch, M., 1999. Lithologic tomography: from plural geophysical data to lithology estimation. J. Geophys. Res. 104, 749–766.

Bott, M.H.P., 1963. Two methods applicable to computers for evaluating magnetic anomalies due to finite three-dimensional bodies. Geophys. Prospect. 11, 292–292.

Brun, J.-P., Balé, P., 1990. Cadomian tectonics in northern Brittany. The Cadomian Orogeny, D'Lemos, R.S., Strachan, R.A., Topley, C.G. (Eds.), Geol. Soc. London Spec. Pub. 51, 95–114.

Cauvin-Cayet, C., Galdeano, A., Egal, E., Pozzi, J.P., Truffert, C., 2001. Magnetic modelling in the French Cadomian belt (Northern Armorican Massif). Tectonophysics 331 (1–2), 123–144.

Chantraine, J., Egal, E., Thiéblemont, D., Le Goff, E., Guerrot, C., Ballèvre, M., Guennoc, P., 2001. The Cadomian active margin (North Armorican Massif France): a segment of the North Atlantic Panafrican Belt. Tectonophysics 331 (1–2), 1–18.

Chapman, M.E., 1979. Techniques for interpretation of geoid anomalies. J. Geophys. Res. 84, 3793–3801.

Clowes, R.M., Cook, A., Green, A.G., Keen, C.E., Ludden, J.N., Percival, J.A., Quinlan, G.M., West, G.F., 1992. Lithoprobe: new perspectives on crustal evolution. Can. J. Earth Sci. 29, 1813–1864.

D'Lemos, R.S., Strachan, R.A., Topley, C.G., 1990. The Cadomian orogeny in the North Armorican Massif: brief review. In: The Cadomian Orogeny, D'Lemos, R.S., Strachan, R.A., Topley, C.G. (Eds.),.Geol. Soc. Lond. Spec. Pub. 51, 3–12.

Deutsch, C.V., Journel, A.G., 1992. GSLIB, Geostatistical Software Library and User's Guide. Oxford University Press, New York, 340 pp.

Edel, J.B., Weber, K., 1995. Cadomian terranes, wrench faulting and thrusting in the central Europe Variscides: geophysical and geological evidence. Geol. Rundsch. 84, 412–432.

Emmermann, R., Lauterjung, J., 1997. The German continental deep drilling program KTB: overview and major results. J. Geophys. Res. 102, 18 179–18 201.

Galdeano, A., Asfirane, F., Truffert, C., Egal, E., Debeglia, N., 2001. The aeromagnetic map of the French Cadomian belt. Tectonophysics 331 (1–2), 99–122.

Hastings, W.K., 1970. Monte Carlo sampling method using Markov chains and their applications. Biometrika 57, 97–109.

Horen, H., 1997. Proprietés magnétiques et sismiques de la lithosphère océanique, à partir d'échantillons marins et d'analogues ophiolitiques, vol. VII. Doctoral Thesis, University of Paris, 350 pp.

Le Borgne, E., Le Mouël, J.L., 1969. La nouvelle carte magnétique de la France. Ann. Inst. Phys. Globe Paris 35, 197–224.

Le Mouël, J.L., 1969. Sur la distribution des éléments magnétiques en France. Doctoral thesis, University of Paris.

Groupe de Recherche GeoFrance 3D, Ledru, P., 1997. GéoFrance 3D: l'imagerie géologique et géophysique 3D du sous-sol de la France. Mem. Soc. Géol. Fr. 172, 53–71.

Metropolis, N., Rosenbluth, A.W., Rosenbluth, M.N., Teller, A.H., Teller, E., 1953. Equation of state calculations by fast computing machines. J. Chem. Phys. 21, 1087–1092.

Mosegaard, K., Tarantola, A., 1995. Monte Carlo sampling of solutions to inverse problems. J. Geophys. Res. 100, 12 431–12 447.

Tierney, L., 1994. Markov chains for exploring posterior distributions. Ann. Stat. 22, 1702–1762.

Treloar, P.J., Strachan, R.A., 1990. Cadomian strike-slip tectonics in NE Brittany. The Cadomian Orogeny., D'Lemos, R.S., Strachan, R.A., Topley, C.G. (Eds.), Geol. Soc. Lond. Spec. Pub. 51, 151–168.

Truffert, C., Egal, E., LeGoff, E., Courrioux, G., Guennoc, P., 2001. Gravity modelling of the Cadomian active margin of northern Brittany. Tectonophysics 331 (1–2), 81–97.